Monthly Notices
of the
ROYAL ASTRONOMICAL SOCIETY

MNRAS **482,** 1757–1785 (2019)
Advance Access publication 2018 October 11

doi:10.1093/mnras/sty2743

Period spacings of γ Doradus pulsators in the *Kepler* field: detection methods and application to 22 slow rotators

Gang Li,[1,2]★ Timothy R. Bedding,[1,2]★ Simon J. Murphy,[1,2] Timothy Van Reeth,[1,2] Victoria Antoci[2] and Rhita-Maria Ouazzani[3]

[1]*Sydney Institute for Astronomy (SIfA), School of Physics, The University of Sydney, NSW 2006, Australia*
[2]*Stellar Astrophysics Centre, Department of Physics and Astronomy, Aarhus University, Ny Munkegade 120, 8000 Aarhus C, Denmark*
[3]*LESIA, Observatoire de Paris, PSL Research University, CNRS, Sorbonne Universités, UPMC Univ. Paris 06, Univ. Paris Diderot, Sorbonne Paris Cité, 5 place Jules Janssen, 92195 Meudon, France*

Accepted 2018 October 5. Received 2018 October 3; in original form 2018 May 28

ABSTRACT

In γ Doradus (γ Dor) stars, the g-mode period spacing shows an approximately linear relation with period. The slope is a new asteroseismic diagnostic, related to the rotation rate and the azimuthal order m. We report two automated methods, the 'moving-window Fourier transform' and the 'cross-correlation', to detect and measure the period spacings based on 4-yr light curves from the *Kepler* satellite. The results show that the cross-correlation method performs better at detecting the period spacings and their slopes. In this paper, we apply our method to 22 γ Dor stars with g-mode multiplets split by rotation. The rotation periods are similar to the g-mode period spacings, causing the multiplets to overlap. To clarify the overlapping patterns, we use the échelle diagram and introduce a 'copy-shift' diagram to discern and measure the splittings. The first observational relation between slopes and splittings is shown. The slope deviates from zero when the splitting increases, as the theory predicts. We found that what appears to be rotational splittings in two stars is in fact caused by two nearly identical overlapping patterns from binaries.

Key words: asteroseismology – stars: rotation – stars: variables: general.

1 INTRODUCTION

Gravity modes provide a successful way to study the internal structure of stars including the chemical gradient, differential rotation from the core to the surface, and angular momentum transport (e.g. Miglio et al. 2008; Bouabid et al. 2013; Ouazzani et al. 2018). The applications to white dwarfs and subdwarf B stars have been successful due to the suitable frequency range for both ground and space telescopes (e.g. Reed et al. 2011; Su et al. 2014). However, detailed analysis of g modes in main-sequence stars (slowly pulsating B stars and γ Doradus stars), only became available recently (e.g. Kurtz et al. 2014; Pápics et al. 2015, 2017; Van Reeth et al. 2015a; Guo et al. 2017), with great help from the 4-yr *Kepler* mission (Borucki et al. 2010).

γ Doradus (γ Dor) stars are a class of pulsating variables (e.g. Balona, Krisciunas & Cousins 1994; Kaye et al. 1999). They have masses from about 1.3 to 2.0 $M_\odot$ and spectral types A7-F5 and are located near the red edge of the δ Sct instability strip in the Hertzsprung–Russell (H-R) diagram. The mass range covers the boundaries between low-mass stars possessing radiative cores with convective envelopes and high-mass stars that have convective cores and radiative envelopes.

Stellar rotation affects the evolution of all stars but is still poorly understood, such that it is usually neglected in 1D stellar computations. Due to the lack of magnetic braking, rapid rotators are typical among the intermediate-mass main-sequence stars (Royer, Zorec & Gómez 2007). F-type stars have typical projected rotation velocities from 50 to more than 100 km s^{-1} and some A-type stars rotate very rapidly, with $v \sin i \approx$ 120–300 km s^{-1} (Fukuda 1982; Groot, Piters & van Paradijs 1996). γ Dor stars occupy these spectral types hence many should rotate very rapidly, and an accurate stellar model must account for this. The rotational frequency can be close to the pulsation frequency and to the Keplerian break-up rotation rate $\Omega_k = (GM/R_{eq}^3)^{1/2}$, and rotation can therefore change the pattern of period spacings (e.g. Prat et al. 2017).

The pulsations in γ Dor stars are mainly gravity (g) modes, which have buoyancy as the restoring force. The modes are driven by the convective flux blocking at the bottom of the convective envelope (Guzik et al. 2000; Dupret et al. 2004, 2005). They probe the internal stellar structure down to the edge of the convective core. The pulsations have typical periods between 0.3 and 3 d, making them difficult to study from the ground. Shibahashi (1979) deduced that g

★ E-mail: gali8292@uni.sydney.edu.au (GL); tim.bedding@sydney.edu.au (TRB)

modes have period spacings ($\Delta P \equiv P_{n+1,l} - P_{n,l}$) that are constant in a spherical chemically homogeneous non-rotating star if $l \ll n$, where l is the degree and n is the radial order (e.g. Balona 2018). However, breaking of either of these two assumptions, homogeneity and no rotation, results in deviations from the asymptotic formula. A more complete relation was deduced by Miglio et al. (2008). The authors found that a chemical gradient at the edge of the convective core led to a sharp variation (glitch) of the buoyancy frequency and is responsible for a series of dips in the period-spacing pattern. Meanwhile, a homogeneous star, such as a pre-main sequence star, generally shows a regular period spacing (Bouabid et al. 2011).

To take the rotational effect into account, the first-order perturbative approach can be used in slowly rotating stars (Ledoux 1951). The frequency splitting is $\delta\nu = m(1 - C_{n,l})\Omega$, where n is the radial order, l is the degree, m is the azimuthal order, Ω is the rotational frequency, and $C_{n,l}$ is the Ledoux constant. Ballot et al. (2010) discussed the validity of the perturbative approach. They found that the first-order perturbative methods are suited to compute the gravity mode frequencies up to rotation speeds of $\sim$50 km s^{-1} for typical γ Dor stars within the *CoRoT* frequency precision (Baglin et al. 2006). The first-order approach is less valid when we take into account the very good frequency accuracy of the *Kepler* data.

Another method to treat the rotational effect is the traditional approximation of rotation (TAR; e.g. Townsend 2003). Under the TAR, the period spacings are related to the variable eigenvalues from the Laplace tidal equation. The period spacing ΔP is generally a linear function of period P in the inertial reference frame, and the slope $\Sigma \equiv \mathrm{d}\Delta P/\mathrm{d}P$ of a spacing pattern depends on the azimuthal order m. The retrograde modes (here with $m < 0$) generally show upward patterns (i.e. $\Sigma > 0$) while patterns of prograde ($m > 0$) and zonal modes are downwards (Bouabid et al. 2013). The slope Σ strongly correlates with the internal rotation. Ouazzani et al. (2017) established the quantitative relation between Σ and the internal rotational rate, and measured it successfully in several *Kepler* stars, allowing them to determine the internal rotation rates.

The complex pattern of sloping period spacings with glitches makes the automated detection of period spacings in γ Dor stars challenging. About 70 examples have already been presented (e.g. Bedding et al. 2015; Van Reeth et al. 2015a,b; Christophe et al. 2018; Van Reeth et al. 2018; Saio et al. 2018a), and a handful of objects have been analysed in detail (see, Chapellier et al. 2012; Kurtz et al. 2014; Keen et al. 2015; Saio et al. 2015; Schmid et al. 2015; Murphy et al. 2016a). To extract the slopes and period spacings of a much larger sample, we developed an automated method. Section 2 presents the light-curve reduction and the frequency extraction. Section 3 introduces the wavelet algorithm, which was only partly successful. Section 4 gives the details of the cross-correlation method and an Markov Chain Monte Carlo (MCMC) algorithm. The algorithm in Section 4 works better, so we use the cross-correlation method to detect the pulsation patterns. In Section 5, the detection results are reported. We present two stars as examples to show how our code works, and then implemented it on 22 stars that have rotational splittings. For each star showing rotational splittings, we investigated their slopes and splittings to seek observational evidence that the rotation changes the period-spacing pattern.

2 LIGHT-CURVE REDUCTION

We used 4-yr *Kepler* long-cadence (LC; 29.45-min sampling) light curves from the multiscale MAP data pipeline (Stumpe et al. 2014). In each quarter, the light curve was divided by a second-order polynomial fitting to remove the slow trend. The outliers were also deleted if the difference to the polynomial fitting was larger than 5σ. We calculated the Fourier transforms (FTs) of the light curves to get the relation between the fractional amplitude and the frequency. The data have a remarkable frequency resolution of δf =0.000 68 d^{-1}, suitable for analysis of the g modes. Because g modes are asymptotically equally spaced in period, rather than frequency, we inverted the frequency domain to plot the FTs against period (in days), with the variable period resolution of $\delta P = P^2 \delta f$. The period resolution is worse in the long-period region, and the pulsation period for prograde modes in the inertial frame can be shorter due to the fast rotation, hence we investigated the patterns of g modes between 0.2 and 2 d, corresponding to the period resolution from 2.42 to 242 s.

We used an iterative pre-whitening method to extract frequencies. In each iteration, the FT was calculated and the initial frequency corresponding to the largest amplitude was selected. We used a sine function with the initial frequency and amplitude to fit the light curve in order to optimize the frequency in the time domain. Then the fitting residual became the input light curve in the next iteration. The signal-to-noise ratio (S/N) is defined as the amplitude divided by the median value of the amplitude spectrum within 0.2 d^{-1}. We extracted peaks until the S/N was smaller than 3, instead of 4 from the standard criterion (Breger et al. 1993). When subtracting high-amplitude peaks, the background level decreases significantly because the spectral window is removed along with the peak itself. The S/N was calculated based on the final noise level.

The frequency uncertainty is given by

$$\sigma(f) = 0.44 \frac{\langle a \rangle}{a} \frac{1}{T}, \tag{1}$$

where $\langle a \rangle$ is the noise level in the amplitude spectrum, a is the amplitude of peak, and T is the total time span of the data (Montgomery & Odonoghue 1999; Kjeldsen 2003). For the *Kepler* data, $T \simeq 1470$ d. We extracted the peaks down to S/N = 3, so the frequency uncertainty is smaller than 1×10^{-4} cd^{-1}. The peaks with low S/N are still convincing if they follow clear pulsation patterns.

3 WAVELET-LIKE ANALYSIS

In this section, we briefly describe our attempt to use the moving-window FT to detect period-spacing patterns. The algorithm is based on the quasi-linear variation of g-mode period spacings ΔP with period. Therefore, we can extract the quasi-periodic signal ΔP from peaks by calculating the FT in a moving window.

A Gaussian function $G(P_c, \sigma, P) = \exp\left[-\frac{1}{2}\left(\frac{P-P_c}{\sigma}\right)^2\right]$ was used as the window, which was specified by central period P_c and the width σ. We calculated the discrete Fourier transform of the product of the window $G(P_c, \sigma, P)$ and the amplitude spectrum $O(P)$. This wavelet spectrum represents the periodic intensity $I(P_c, \Delta P)$ of the amplitude spectrum around the central period. We can inspect the periodicity by moving P_c. The schematic explanation of the process can be seen in Fig. 1. Windowing with a Gaussian decreases the length of the amplitude spectrum, and thereby permits period resolution, but it degrades the period-spacing resolution. The width of the Gaussian must be chosen appropriately to balance these two resolutions, so we tried three choices of σ (777, 1555, and 3110 s) for each star, which are 0.5, 1, and 2 per cent of the period span (0.2–2 d). These choices cover the typical period-spacing regions.

The function $I(P_c, \Delta P)$ is two dimensional and well represented by a heat map. Fig. 2 depicts the analysis of KIC 4253413, for which Bedding et al. (2015) reported a linear period-spacing pattern. Consequently, it was used as a test of our code. The width was set

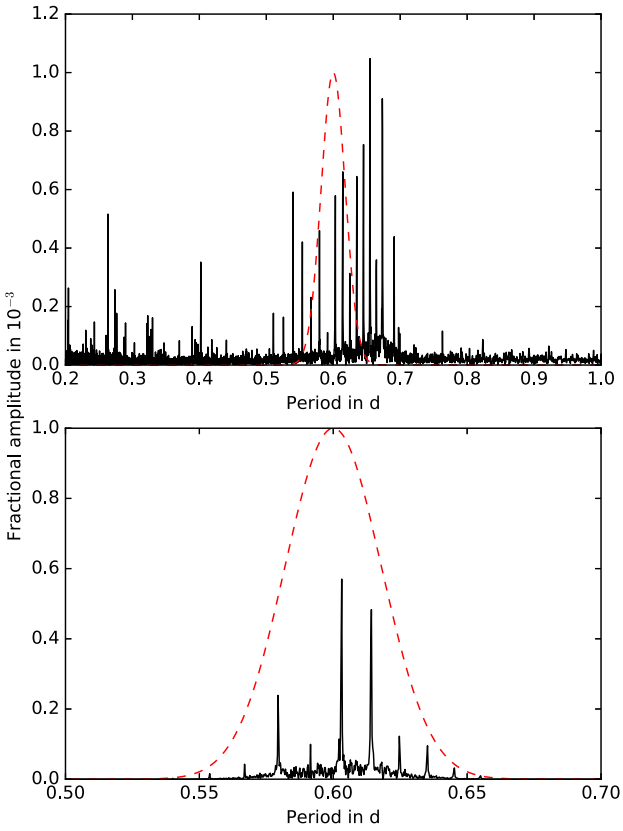

Figure 1. Schematic explanation of the wavelet algorithm. KIC 4253413 is used as a model. Top: the amplitude spectrum $O(P)$ (solid lines) and the window $G(P_c, \sigma, P)$ (dashed lines). Bottom: the product of spectrum and window.

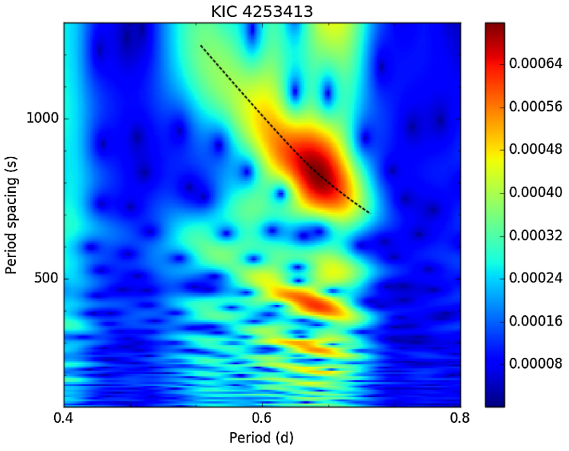

Figure 2. Wavelet analysis of KIC 4353413. The colour denotes $\sqrt{I(P_c, \Delta P)}$, in which the square root is used to enhance the contrast. The significant signal appears around $P \sim 0.65$ d and $\Delta P \sim 800$ s as expected, shown by the black dash line. Other islands of red are harmonics.

as $\sigma = 1555$ s. The expected signal appears around $P \sim 0.65$ d and $\Delta P \sim 800$ s seen as the dominant red area marked by the black dash line. Several harmonics at $\Delta P/2$, $\Delta P/3$ etc. are also seen. The red areas have a downward trend, indicating that the period spacing decreases with period.

However, the disadvantage of the moving-window FT emerged after testing more targets: the resolution of period spacing is low, and the slope cannot be derived directly. In the next section, we will introduce the cross-correlation analysis, which shows a higher sensitivity and accuracy.

4 CROSS-CORRELATION ANALYSIS

In this section, we describe an algorithm based on cross-correlation and MCMC to detect variable period-spacing patterns. The main idea is to build a template pattern and calculate its product with the amplitude spectrum. After maximizing the product, the parameters of the template reveal the period spacing and the slope. This method can give the period spacing and slope directly and accurately, minimizing the impact of the missing peaks. This method is similar to the 'comb response' algorithm used in the analysis of solar-like oscillations (e.g. Kjeldsen et al. 1995). The aim of this work is to automatically identify γ Dor stars that have regular patterns. Once they are found, a more detailed analysis can be done on individual stars.

4.1 Combination frequencies

Combination frequencies are often seen in γ Dor stars, which complicates the detection of period-spacing patterns (see an example in Keen et al. 2015). So it is helpful to first remove these combinations. They can be identified using

$$|f_k - (n_i f_i + n_j f_j)| < \varepsilon, \quad (2)$$

where i, j, k are indices of peaks, f_i and f_j are parent frequencies, f_k is the combination frequency candidate, n_i and n_j are the combination coefficients, and ε is the criterion threshold. For each star, we considered the 20 highest peaks as the parent frequencies and only considered combinations where $|n_i| + |n_j| \leq 2$. We show the distribution of the difference $|f_k - (n_i f_i + n_j f_j)|$ from 1371 *Kepler* stars in Fig. 3. The distribution in Fig. 3 has grey excess over the background. The background shown by the grey dashed line reflects the probability of the random match. The excess is most likely caused by the real combination frequencies. The black dotted line shows three times the background, intersecting the histogram at 0.0002 d^{-1}. That means the probability of that match is a genuine combination frequency in the grey area is at least 67 per cent. Based on this, we selected $\varepsilon = 0.0002\ d^{-1}$ as the threshold.

Fig. 4 presents the amplitude spectrum of KIC 2450944, in which

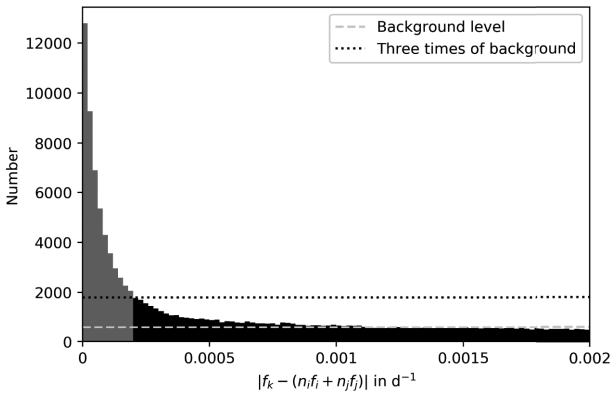

Figure 3. The distribution of frequency differences $|f_k - (n_i f_i + n_j f_j)|$. The excess on the left is evidence of real combination frequencies over random matches. Thepercentage of the real combination frequencies over the random background in the grey area is larger than 67 per cent.

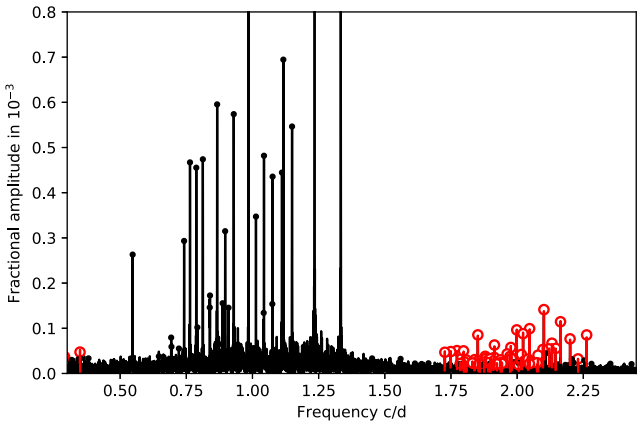

Figure 4. The g-mode amplitude spectrum of KIC 2450944. The solid dots denote the frequencies detected from pre-whitening. The red lines and open circles stand for the frequencies that are combinations. Mode identification can be seen in Fig. A1.

the likely combinations are plotted by red open circles and red lines. The peaks show two main 'frequency groups', the left one is dominated by the parent frequencies while the right one is mainly composed of the combinations. However, because of the large number of detected frequencies, there is a chance that independent modes can also satisfy the combination criterion (Pápics 2012). As pointed out by Saio et al. (2018b), this often happens in rapidly rotating stars where successive frequency groups can be prograde sectoral modes ($m = l$) of increasing degree, and make the detection of combinations tricky. The conclusions of this paper are not affected since the identification of likely combinations is only done to improve the process of correlating with the template. In the final analysis, we look at the overall patterns to decide which peaks are genuine modes.

After pre-whitening the combination frequencies, the spectra were ready to be inspected for g-mode patterns.

4.2 Mathematical formulism of period spacings

In our work, the main goal is to measure the rate of change of the period spacing with respect to period, which we call the 'slope'. In the observations, the signature of chemical gradients in the stellar interior is minor compared to that of the stellar rotation among published examples (e.g. Van Reeth et al. 2015a). Even if there is a dip, the pattern can be recognized as two patterns separated by the dip. Hence, we do not include dips caused by chemical gradients in our template.

The asymptotic formula gives the relation between the period and radial order (Shibahashi 1979; Tassoul 1980)

$$P_n = \Delta P \left(n + \epsilon_g\right). \tag{3}$$

In that case, the slope is zero since the period spacing is constant. However, we assume that the period spacing ΔP depends linearly on the period P, then the relation between the period spacing and the period P can be written as

$$\Delta P = \Sigma\, P + b, \tag{4}$$

in which Σ is the slope and b is the intercept.

Now we present a new formula to calculate P after eliminating ΔP. The intercept b in equation (4) can be determined from one particular period P_0 and its corresponding period spacing ΔP_0 so that the linear relation can be written as

$$\Delta P = \Sigma\, P + \Delta P_0 - \Sigma\, P_0. \tag{5}$$

Two adjacent period values P_i and P_{i+1} are related as

$$P_{i+1} = P_i + \Delta P_i = (1 + \Sigma)\, P_i + \Delta P_0 - \Sigma\, P_0, \tag{6}$$

in which i is an integer. Therefore, the analytic expressions of ΔP_i and P_i are derived as

$$\Delta P_i = (1 + \Sigma)^i\, \Delta P_0 \tag{7}$$

and

$$P_i = \sum_{j=0}^{i-1} \Delta P_j + P_0 = \Delta P_0\, \frac{(1 + \Sigma)^i - 1}{\Sigma} + P_0. \tag{8}$$

Equation (7) reveals that the series of period spacings varies as a geometric sequence with the common ratio of $1 + \Sigma$, which is a new meaning of Σ.

Although equation (8) is invalid when $\Sigma = 0$, which corresponds to the non-rotating case, the limit is still valid

$$P_i = \lim_{\Sigma \to 0} \Delta P_0\, \frac{(1 + \Sigma)^i - 1}{\Sigma} + P_0 = i\, \Delta P_0 + P_0.$$

Hence, the limit when $\Sigma \to 0$ can describe the non-rotating equally spaced case.

Equation (8) can be written as

$$P_i = \Delta P_0 \left(\frac{(1 + \Sigma)^i - 1}{\Sigma} + \epsilon_g\right), \tag{9}$$

which is an extension of traditional asymptotic relation $P_n = \Delta P(n' + \varepsilon_g)$, where $n' = \frac{(1+\Sigma)^i - 1}{\Sigma}$. Using equation (8) with given periods and their integers i, the first period spacing ΔP_0 and the slope Σ can be derived by fitting. The advantage is that we can fit a period series by giving the indices i, even when a lot of peaks are missing and the period spacing cannot be calculated directly. However, when too many peaks are missing, assignment of the series index becomes ambiguous and a unique fit is not possible.

4.3 The template

In order to avoid the problem of ambiguous index assignment caused by the missing peaks, we used a template to find the parameters of the pattern. Considering that the peaks in γ Dor stars generally cluster into several groups (Kurtz et al. 2015), the template $T(\nu)$ was designed to detect the pattern centred around the highest amplitude peak in each group. Fig. 5 shows the template. It is comprised of a series of narrow parabola functions with uniform amplitude. We chose a parabola over a more complicated function, such as a Gaussian or a sinc, to improve computation speed. Five parameters are needed to specify the template: the central period P_c, the period spacing ΔP_c at P_c, the slope Σ, the number of peaks N_l on the left of P_c (including P_c), and the number of peaks N_r on the right of P_c (excluding P_c). The full-width at zero-amplitude of each parabola is fixed as 100 s, which becomes the lower limit of the period spacing we can detect. The lower limit is deliberately much larger than the period resolution mentioned in Section 2 because they have different meanings: the full width allows the template to tolerate some dips and scatters in the observed period-spacing patterns, considering the linear relation between the period spacing and period is not strict. The amplitude of the parabola is arbitrary since it cancels in the fraction of the likelihood function (equation 10).

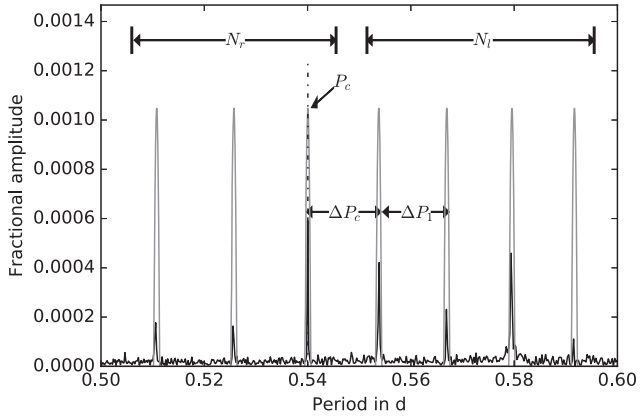

Figure 5. The example of template for KIC 4253413 (the grey lines), which best matches the power spectrum (black lines). The parameters are: $P_c = 0.54$ d, $\Delta P_c = 1183$ s, $\Sigma = \Delta P_1/\Delta P_c - 1 = -0.041$, $N_l = 3$, and $N_r = 4$.

4.4 Cross-correlation and MCMC

The cross-correlation of the template with the observed amplitude spectrum represents the goodness of fit. If the template matches the observed power spectrum very well, the value should be large, otherwise, it will be close to zero because the peaks in the template line up with the noise in the spectrum, rather than the observed peaks. In this method, any missing peaks do not influence the results greatly.

We define the likelihood function, given the observed spectrum and five parameters, as

$$L(\text{data}|P_c, \Delta P_c, \Sigma, N_r, N_l) = \left[\frac{\int T(\nu)O(\nu)\,\mathrm{d}\nu}{\int T(\nu)\,\mathrm{d}\nu}\right]^{\beta}, \quad (10)$$

where $T(\nu)$ stands for the template, $O(\nu)$ is the power spectrum in unit of frequency ν, and β is the tampering parameter. The parameter β changes the gradient of the likelihood function, which can enhance the convergence or guide the chain to the global minimum. We tested several choices of β and found the convergence to be best when $\beta = 7$.

A special prior was designed as

$$P(P_c, \Delta P_c, \Sigma, N_r, N_l) = \frac{N_r N_l}{\Delta P}. \quad (11)$$

There are two reasons for such a design: to find the fundamental period spacing rather than a harmonic, and to find longer patterns. Considering that a series of periods $\{P_i, i = 0, 1, 2, \ldots\}$ forms a pattern that satisfies the equation (8), a new series $P_i' = P_{2i}$ that takes every second point also roughly obeys the equation (8) with twice spacing $\Delta P' = 2\Delta P$ and twice slope $\Sigma' = 2\Sigma$. The prior in equation (11) is designed to distinguish the fundamental spacing ΔP and the harmonic $\Delta P'$. They have the same likelihood value but can be clarified by the prior.

Finally, the posterior probability, given certain parameters (P_c, ΔP_c, Σ, N_r, N_l), is

$$P(P_c, \Delta P_c, \Sigma, N_r, N_l|\text{data}) = \frac{N_r N_l}{\Delta P_c}\left[\frac{\int T(\nu)O(\nu)\,\mathrm{d}\nu}{\int T(\nu)\,\mathrm{d}\nu}\right]^{\beta}. \quad (12)$$

In order to enhance the convergence of MCMC chains, we set the amplitudes of all the independent peaks in the power spectrum equal to the maximum amplitude and set the amplitudes of combination frequencies and noise to be zero. Since the peaks are generally clustered into groups, we analysed them with a 1D k-means clustering algorithm (MacQueen 1967; Wu 2010), which is a common and

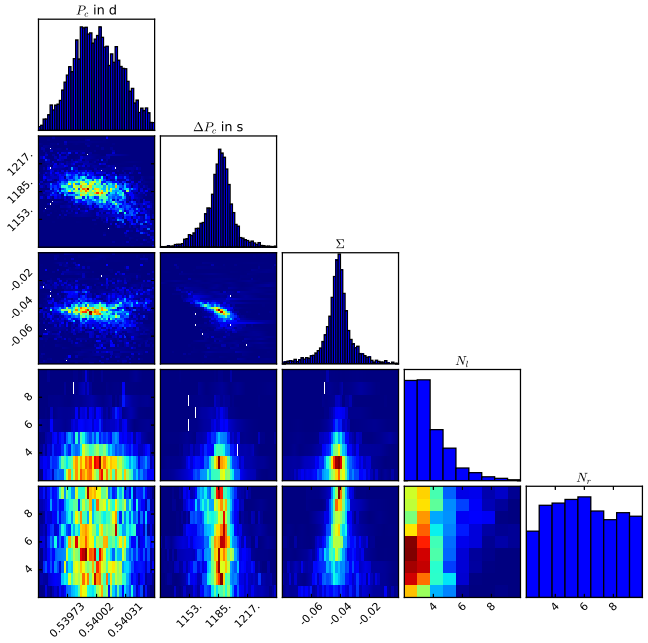

Figure 6. The posterior distributions of KIC 4253413 based on equation (12). The significant signal appears around $\Delta P \approx 1100$ s and $\Sigma = -0.04$. Axis labels are given above each column.

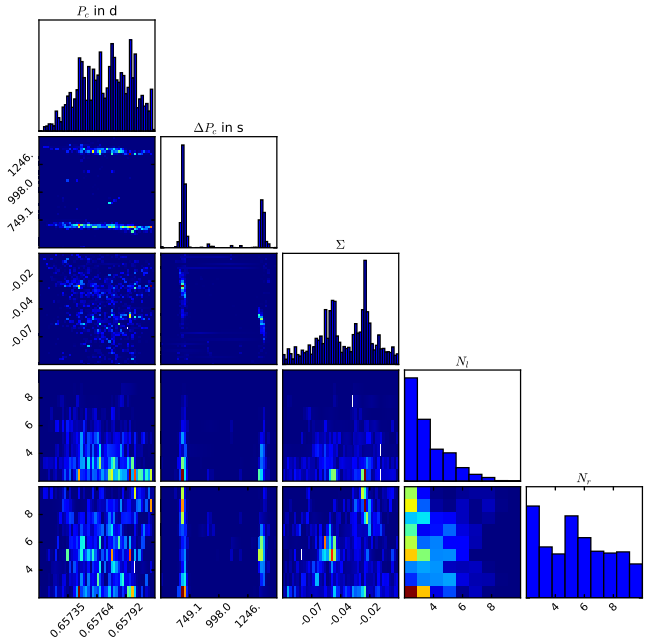

Figure 7. Same as Fig. 6 but for KIC 3331147. Note that there are two peaks in the frames of period spacing and the slope. The one with higher posterior ($\Delta P = 740$ s, $\Sigma = -0.025$) corresponds to the correct solution.

powerful clustering algorithm used in unsupervised machine learning (see two applications in Giri, Mellema & Ghara 2018; Rahmani, Teimoorinia & Barmby 2018). We used six frequency groups and in each group we included the pattern around the highest peak if the number of independent frequencies within the group was larger than four, since there are three free parameters in equation (8) (P_0, ΔP_0, and Σ). The sampling range of the central peak was set to be

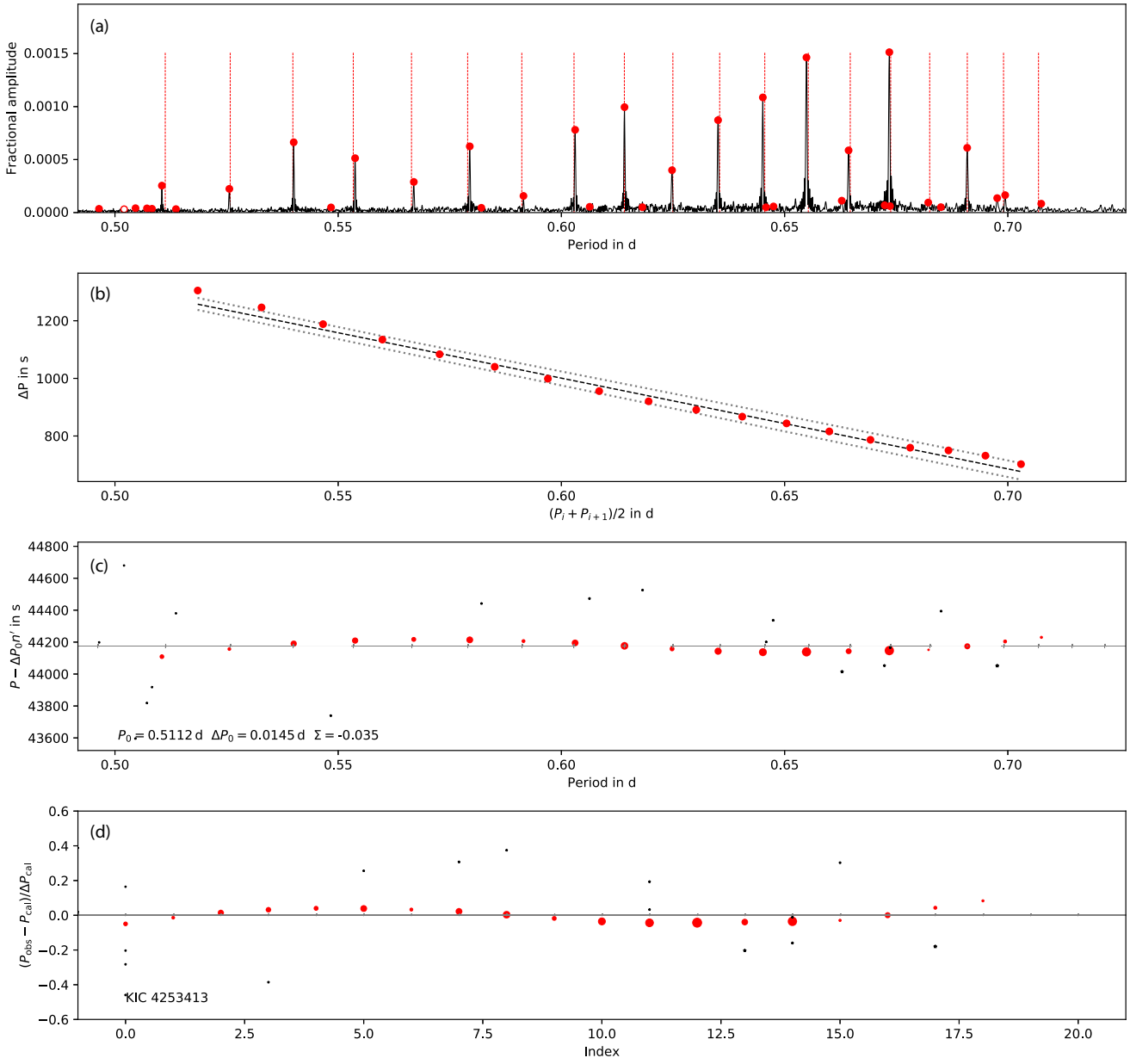

Figure 8. The amplitude spectrum and period-spacing pattern of KIC 4253413. Top panel: the amplitude spectrum. The grey dashed lines show the best-fitting results for a linearly varying period spacing. The solid red circles are the peaks from pre-whitening and the open red circles show combinations. Second panel: the period-spacing pattern. The red circles are the observed data, for each circle two adjacent peaks P_i and P_{i+1} are detected so that $\Delta P_i = P_{i+1} - P_i$ can be calculated. The x-coordinate of each solid red circle is $\frac{P_i + P_{i+1}}{2}$. The slope of this pattern is $\Sigma = -0.0358 \pm 0.0006$. Third panel: sideways échelle diagram, where circles are peaks that fit the period-spacing patterns and black stars show peaks that do not. Symbol size is proportional to peak amplitude. Fourth panel: same as the third panel, but with x-axis rescaled so that the points are equally spaced.

$P_p \pm 3\delta P$, where P_p is the highest peak in each frequency group and δP is the period resolution. The ranges for the other four free parameters were ΔP from 100 to 4000 s, Σ from 0.2 to -0.2, N_l and N_r from 2 to 10. The EMCEE package in PYTHON was used to implement the MCMC algorithm (Foreman-Mackey et al. 2013). We used 20 parallel chains and the chain length was set to be 2400. The parameters were derived after maximizing the posterior. Since the posterior distributions may be multimodal (see the example in Fig. 7), we used k-means clustering again in five-dimensional space $(P_c, \Delta P_c, \Sigma, N_l, N_r)$ to cluster the chain points into two groups. The medians of the group with the most points were used as the MCMC results.

The results from MCMC gave a good initial guess on the series indices i. However, our likelihood function is not defined by the conditional probability, so the distributions do not represent the uncertainties. To derive the uncertainties of P_c, ΔP, and Σ, the parameters were optimized further based on minimizing χ^2 between the observed period series and the prediction from the equation (8),

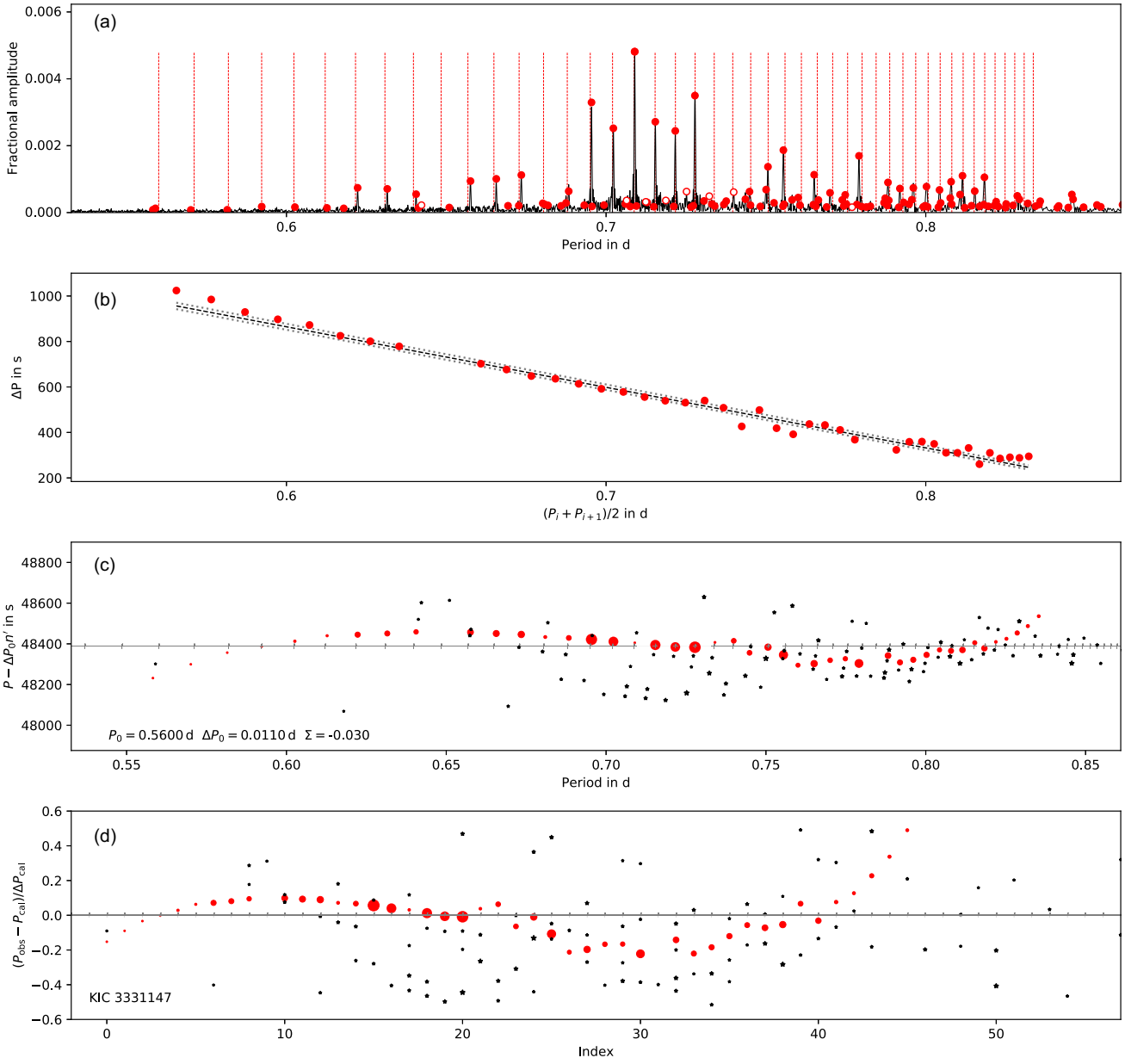

Figure 9. Same as Fig. 8 but for KIC 3331147. The slope of this pattern is $\Sigma = -0.0307 \pm 0.000\,02$.

defined as

$$\chi^2 = \sum_i \left(P_i^{\rm cal} - P_i^{\rm obs}\right)^2, \tag{13}$$

where $P_i^{\rm cal}$ is the period calculated from the template and $P_i^{\rm obs}$ the observed one. The patterns were finally checked and confirmed by eye.

5 ANALYSIS OF *Kepler* γ DOR STARS

We visually inspected the FTs of 4-yr light curves of 1371 *Kepler* targets with an effective temperature from 6600 to 10 000 K, including 339 δ Scuti binaries detected by the pulsation timing method (Murphy et al. 2018). Among the binary systems, either the δ Scuti companion or its companion could show g-mode pulsations, and in some cases both stars do (e.g. Keen et al. 2015; Guo et al. 2017). We found ∼500 stars showing clear period-spacing patterns. We identified 22 stars in which possible rotational splittings are seen and applied the algorithm to measure the slopes. The splittings are approximately proportional to the rotational rates, therefore the relation between the slope and the rotational rates can be revealed in different m.

5.1 Posterior distributions of two examples

KIC 4253413 is again used for illustrating our code. Fig. 6 displays the one- and two-dimensional projections of the posterior distributions. It shows that there is a significant detection around $\Delta P \approx 1185$ s and $\Sigma = -0.04$. The distributions of N_r and N_l are asymmetric because the strongest peak does not lie in the centre of the excited distribution. N_r and N_l cannot cover the whole pattern in some cases, which is caused by the deviation from the linear

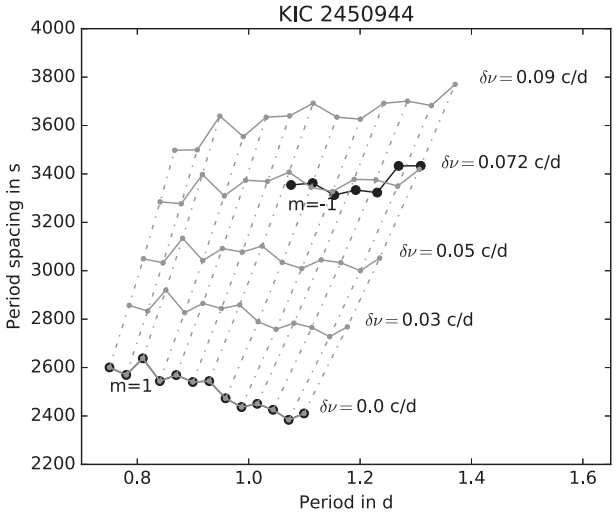

Figure 10. This copy-shift diagram shows how we identify the unclear splittings, using KIC 2450944 as example. The black circle show the two observed patterns, while the grey points show the shifted copies of $m = 1$ modes with different splittings. The dashed lines connect the modes with same radial order.

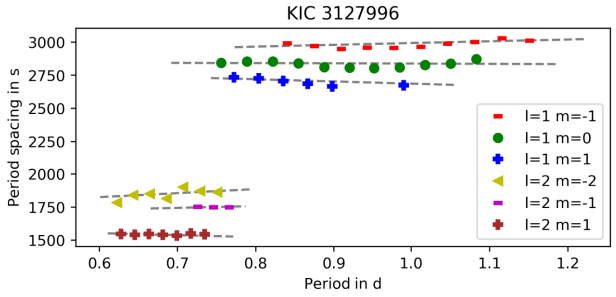

Figure 11. The observational and theoretical period-spacing patterns of KIC 3127996.

model (equation 8), similar to the curvature in the échelle diagram of solar-like oscillators (e.g. fig. 1.2 in Bedding 2014).

Fig. 7 shows our results for KIC 3331147. The period-spacing harmonics are significant so that it is an opportunity to see how the MCMC algorithm performs when searching for the fundamental period spacing. The posterior distributions in Fig. 7 give two peaks, corresponding to ΔP and $2\Delta P$. Thanks to the prior $1/\Delta P$ included in equation (11), the ones with higher probabilities are the correct period spacing and slope. From this example, we see that our code has the ability to avoid the influence of missing peaks and to find the correct period spacing in an incomplete pattern.

The corresponding period-spacing patterns of these two stars can be seen in Figs 8 and 9. The first panel shows the amplitude spectrum. The vertical dashed lines are the peaks' locations from the best-fitting model assuming the period spacing varies linearly (equation 8). The second panel depicts the observed and best-fitting period spacings. We only plot the period spacings that can be calculated by two adjacent peaks, as shown in red solid circles in the second panel. Since these spacings are calculated from two peaks, we used the mean period $\frac{P_i+P_{i+1}}{2}$ as their x-coordinates in the second panels of Figs 8 and 9. The black dashed line is the best-fitting result, while the grey dotted lines show the $\pm 1\sigma$ region. The values for the slopes are $\Sigma = -0.0358 \pm 0.0006$ for KIC 4253413 and -0.0307 ± 0.00002 for KIC 3331147.

Considering the formula $P_i = \Delta P(n' + \varepsilon_g)$ from the equation (9), we can plot the period échelle diagrams analogous to the traditional échelle diagram, which is often used for solar-like oscillators. In the third panel of Fig. 8, the y-axis is the difference between the observed period $P_{\rm obs}$ and the term $\Delta Pn'$ while the x-axis is the period. This is therefore a 'sideways' échelle diagram. For the peaks that fit the pattern, we can calculate the value $P_{\rm obs} - \Delta Pn'$ accurately and plot them as red circles. For the peaks that do not belong to any pattern, we find the value n' that minimizes $|P_{\rm obs} - (\Delta Pn' + \Delta P\varepsilon_g)|$, shown in black stars. The échelle diagram of KIC 4253413 (third panel of Fig. 8) shows a clear fluctuation around $\Delta P\varepsilon_g$, implying deviations from the linear functional form.

The fluctuation indicates the change of slope, which is not an exact constant for a real star. Some of the fluctuations are most likely caused by the Coriolis force and the change from the co-rotating to the inertial reference frame. In addition, pulsation mode trapping, caused by chemical gradients in the stellar interior, also results in changes in the slope of the pattern. Usually, fluctuations in a period-spacing pattern caused by mode trapping are the most pronounced (e.g. Bouabid et al. 2013).

The y-axis term $P_{\rm obs} - \Delta Pn'$ in the third panel is always smaller than half of the local spacing and decreases with period. Also, the points along x-axis become denser. To remove the influence from the changing period spacings, we plot the normalized diagram in the fourth panel in Fig. 8. The y-axis is normalized by the period spacing ΔP hence the meaning of the y-axis is thepercentage deviation. The x-axis is the index of peaks, counted from the first peak in the pattern. This normalized diagram makes it easy to compare between different stars since the effect from changing period spacing is eliminated.

5.2 Slow rotators

Several examples of slowly rotating γ Dor stars have been reported such as KIC 11145123 (Kurtz et al. 2015), KIC 9244992 (Bedding et al. 2015; Saio et al. 2015), KIC 3127996 (Bedding et al. 2015), KIC 7661054 (Murphy et al. 2016a), and KIC 10080943 (Keen et al. 2015). In these cases, clear doublets or triplets are observed and the rotation rates of their cores can be calculated with model independence. The observed rotation rate is smaller than expected from both observations and theories for A-type stars, implying some new mechanism of angular momentum transport operates in these stars (Ouazzani et al. 2018, submitted). It is a challenge for current stellar structure and evolution theory.

As pointed out by Ouazzani et al. (2017), the slope defined as $\Sigma = {\rm d}\Delta P/{\rm d}P$ is a diagnostic of the internal rotation. To investigate this diagnostic without model dependence, we applied our algorithm to 24 γ Dor stars in which splittings are seen. The internal rotation can be calculated from the splitting, hence the slope–rotation relation can be tested. Our results show that there are 22 stars whose splittings are caused by rotation, while there are two stars, KIC 6862920 and KIC 8458690, whose apparent splittings are two overlapping patterns from a binary, instead of the rotational effect. Results for all 24 stars are shown in the appendix.

5.2.1 Splitting identification

We use KIC 2450944 as the example to illustrate the process. Fig. A1 depicts two uniformly spaced overlapping patterns. It seems likely that these two patterns are the result of rotational splittings. However, due to the relatively large splitting and the absence

Table 1. The slopes and splittings of 22 slowly rotating stars collected from this paper and previous literature. KIC 10080943 is a binary, whose components are marked by A and B. Only $l = 1$ splittings are listed. $\delta\nu$ are the mean splittings. l are the degrees. Σ are the slopes for each m. The uncertainty on the last digit is given between brackets. The final column gives references to additional studies on the targets.

KIC number	$\delta\nu$ in d^{-1}	l	$\Sigma_{m=1}$	$\Sigma_{m=0}$	$\Sigma_{m=-1}$	Reference
2450944	0.0731(3)	1	− 0.0084(4)		0.003(1)	
3127996	0.0271(1)	1	− 0.0043(4)	− 0.0007(5)	0.0024(4)	Bedding et al. (2015)
3222854	0.0059(1)	2	− 0.0003(3)		− 0.0004(3)	
4480321	0.0041(1)	1	0.0006(3)	− 0.0002(1)	− 0.0001(4)	Lampens et al. (2018)
4919344	0.1055(4)	1	− 0.0221(7)	− 0.0167(3)	− 0.0108(4)	
5038228	0.0801(4)	1	− 0.0116(8)	− 0.0006(7)	0.0041(2)	
5459805	0.060 09(6)	1	− 0.000(2)		0.011(3)	
5557072	0.0020(3)	1	0.0013(3)	0.0020(3)	0.0020(5)	
5810197	0.0427(1)	1	− 0.0066(4)		− 0.006(2)	
6302589	0.0561(1)	1	− 0.006(1)	− 0.012(4)	0.000(2)	
6467639	0.1179(6)	1	− 0.0228(4)	− 0.001(1)	0.0082(2)	
6937123	0.0638(4)	1	− 0.0039(2)	− 0.0007(9)	0.0003(4)	
7661054	0.018 53(4)	1	0.0000(4)		0.0014(4)	Murphy et al. (2016a)
7697861	0.0262(1)	1	− 0.0078(7)		− 0.0018(8)	
8197761	0.001 68(6)	1	0.002(1)	0.000(2)	− 0.005(2)	Sowicka et al. (2017)
9028134	0.093(1)	1	0.001(2)	− 0.000(3)	− 0.0024(6)	
9244992	0.007 89(7)	1	− 0.0022(2)	− 0.0022(2)	0.0002(2)	Saio et al. (2015)
9751996	0.0351(1)	1	− 0.0042(2)	0.001(1)	0.0036(5)	Van Reeth et al. (2015a)
10080943(A)	0.045 55(6)	1	− 0.0028(4)		0.0019(5)	Keen et al. (2015)
10080943(B)	0.0706(2)	1	− 0.0171(8)	− 0.008(1)	0.0024(7)	Keen et al. (2015)
10468883	0.075(1)	1	0.003(2)	0.011(1)	0.024(1)	
11145123	0.0048(1)	1	0.0026(4)	0.001(1)	0.0031(6)	Kurtz et al. (2014)

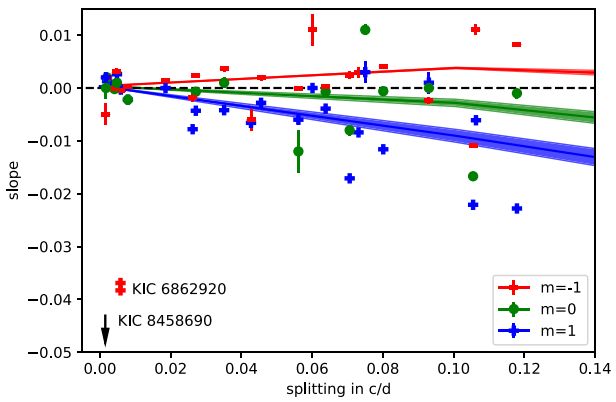

Figure 12. The slope versus splitting diagram from 22 γ Dor stars whose splittings are caused by the rotation effects. The shaded curves are the theoretical prediction from Ouazzani et al. (2017). KIC 6862920 and KIC 8458690 shows two outliers, because their splittings are the two overlapped patterns from both components. We use a downward arrow to note KIC 8458690 since its slope is too small ($\Sigma = -0.08$).

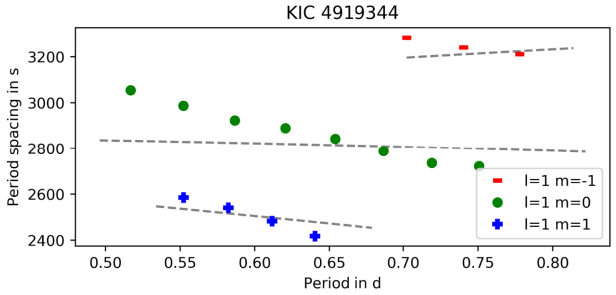

Figure 13. The observational and theoretical period-spacing patterns of KIC 4919344. The fits are poor because these three patterns are parts of dips.

of zonal modes, it is hard to identify the doublets. In order to solve this problem, we identified their degrees as $l = 1$ and azimuthal orders as $m = \pm 1$, respectively, based on the mean period spacings of the observed patterns (e.g. Van Reeth, Tkachenko & Aerts 2016) and the known effects of geometric mode cancellation (e.g. Chadid et al. 2001). We selected the $m = 1$ pattern as the template, tried several splitting values and calculated the shifted copy. Fig. 10 is a 'copy-shift diagram' and it displays the process, in which the grey line with $\delta\nu = 0.072\,\mathrm{d}^{-1}$ fits the $m = -1$ (retrograde) pattern. The retrograde pattern has larger period spacings than those of the prograde pattern. The grey dashed lines in Fig. 10 join the modes with same radial order n. We see that the prograde modes extend to lower n than the retrograde modes.

Since the rotation rates are sufficiently low, we can use the first-order perturbative treatment to obtain the rotational period of the core (Aerts, Christensen-Dalsgaard & Kurtz 2010),

$$P_{\mathrm{c}} = \frac{1 - C_{n,l}}{\overline{\delta\nu}}, \tag{14}$$

where $\overline{\delta\nu}$ is the observed frequency splitting of the g modes. The Ledoux constant $C_{n,l} \approx [l(l+1)]^{-1}$ is fixed to 0.5 without considering its variation with radial order n (Saio 1981). For KIC 2450944, for example, $\overline{\delta\nu} = 0.072\,\mathrm{d}^{-1}$. The rotation period near the boundary of the convective core is therefore determined as 6.9 d.

We identified the doublets from the splitting $\delta\nu = 0.072\,\mathrm{d}^{-1}$, plotting them in the top panel of Fig. A1. The left-hand panel of Fig. A2 presents the échelle diagram of KIC 2450944, where two series are seen. Considering that the Ledoux 'constant' changes slightly and it may give some information about differential rotation, we also investigated the splitting variation with frequency. The right-hand panel of Fig. A2 shows that the splitting increases with frequency and their variation reaches $\sim 6 \times 10^{-4}\,\mathrm{d}^{-1}$, one order of magnitude bigger than the typical frequency uncertainty (for other examples, see also Keen et al. 2015; Murphy et al. 2016a).

Based on 22 stars with rotational splittings, we find that the triplets are slightly asymmetric as expected. The value $f_{m=0} - f_{m=-1}$ is smaller than $f_{m=1} - f_{m=0}$ (see Figs A11 and A13 for examples). This asymmetry is due to the second-order perturbation (as stated in Keen et al. 2015). On the other hand, the splitting generally rises or does not change with increasing frequency for $l = 1$ modes (like Figs A2 and A49). This trends reflect that the Ledoux constant varies slightly as a function of radial order.

5.2.2 Quadrupole modes

In some stars $l = 2$ modes are detected. KIC 3127996 shows splittings both in $l = 1$ and 2 modes (Bedding et al. 2015), but assigning the azimuthal orders to $l = 2$ is not straightforward. Meanwhile, the frequencies of $l = 2$ modes deviate from the perturbative approach at a smaller rotation rate than for $l = 1$ modes. To solve this problem, we used the TAR to build theoretical patterns for KIC 3127996. In the TAR, the period in the corotating frame $P_n^{\rm co}$ is calculated by the formula

$$P_n^{\rm co} = \frac{\Pi_0}{\sqrt{\lambda}} \left(n + \alpha_g\right), \tag{15}$$

where $\Pi_0 = 2\pi^2 \left(\int \frac{N}{r} {\rm d}r\right)^{-1}$ is the asymptotic spacing, N is the Brunt–Väisälä frequency, r is radius, n is the radial order, and the phase term α_g is assumed to be 0.5. Note that λ is the eigenvalue of Laplace's tidal equation, which is related to the rotational rate $\nu_{\rm rot}$, the pulsation frequency in the corotating frame $\nu^{\rm co}$, and the quantum numbers l and m (Lee & Saio 1987; Townsend 2003; Bouabid et al. 2013).

The quadrupole patterns in KIC 3127996 were calculated based on the asymptotic spacing $\Pi_0 = 4028$ s and the rotational rate $\Omega = 0.053\,{\rm d}^{-1}$, which were calculated from the dipole triplets. The eigenvalues λ were read from GYRE's table (Townsend & Teitler 2013). Fig. 11 presents the results from the TAR, in which several possible m choices were tried and $m = \pm 1$ fitted the observational pattern best. Fig. A3 shows the amplitude spectrum and the period-spacing patterns of KIC 3127996. The échelle diagrams and the splitting variations can be seen in Figs A4 and A5 for $l = 1$ and 2 modes, respectively. The splittings are about $0.27\,{\rm d}^{-1}$ for $l = 1$ and $0.45\,{\rm d}^{-1}$ for $l = 2$ modes, whose ratio obeys the theoretical value 0.6 from the Ledoux constant $C_{n,l} = [l(l+1)]^{-1}$.

KIC 5038228 (Fig. A12), KIC 5459805 (Fig. A15), and KIC 6937123 (Fig. A28) also show $l = 2$ patterns. We used the TAR to identify them (see Figs A14, A17, and A31).

5.2.3 Binaries

KIC 6862920 is a PB2 binary system detected by phase modulation by Murphy et al. (2018). Here, 'PB2' means that two stars are pulsating in pressure modes and we can detect the phase motions of both pulsators. The orbital parameters are listed as follows: orbital period $= 61.54^{+0.07}_{-0.07}$ d, eccentricity $= 0.58^{+0.14}_{-0.11}$, $a_1 \sin i/c = 94^{+10}_{-8}$ s, $a_2 \sin i/c = 88^{+14}_{-14}$ s, and mass ratio $M_2/M_1 = 1.1^{+0.20}_{-0.15}$, where a_1 and a_2 are the semimajor axes for two components, i is the inclination and c is the speed of light.

The gravity mode patterns are seen in Fig. A26. The amplitude spectrum shows 'doublets' clearly, causing two parabola curves in the échelle diagram (the left-hand panel of Fig. A27). These two parallel period spacings have slopes of -0.037, which implies that the core rotation is fast enough to deviate from the asymptotic relation. However, as shown in the right-hand panel of Fig. A27, the mean splitting is only $\sim 0.0058\,{\rm d}^{-1}$, which would imply a rotational period of 86 d.

To explain the conflict between the slope and the 'splitting', we assume that those two components with nearly equal masses ($M_2/M_1 = 1.1^{+0.20}_{-0.15}$) have the almost same evolutionary stages. The period-spacing patterns come from two identical components so they look like rotational splittings but actually come from two different stars.

We find that KIC 8458690 is another binary that shows similar patterns. This spectrum has a very small splitting ($\delta\nu = 0.0015\,{\rm d}^{-1}$) but extremely steep slopes $\Sigma = -0.08$ (Figs A38 and A39). These are incompatible and we deduce that there are two γ Dor stars contributing to the spectrum. The mass ratio is $M_2/M_1 = 0.83 \pm 0.29$ (Murphy et al. 2018), also implying that these two patterns are from two components, rather than rotational splittings.

5.2.4 Slope versus splitting

Ouazzani et al. (2017) gave a theoretical relationship between the slope and rotation rate. They found that the slope will decrease to negative values for prograde and zonal modes, and increase for retrograde modes. In order to investigate the observational evidence, we selected 22 slowly rotating targets listed in Table 1. 13 of them are first reported in our sample, while others are from previous literature.

After identifying their period-spacing patterns and rotational splittings, we present the observational slope versus splitting relation in Fig. 12. When the splitting is close to zero, i.e. when the rotation rate is very low, the period spacing is well reproduced by the Shibahashi (1979) asymptotic relation. This predicts a period spacing that is constant a function of period, hence the slope near to zero that we see in Fig. 12. When the splitting rises, the diagram shows more spread. The rotation breaks the asymptotic relation and changes the spacing. The prograde and zonal patterns (shown as circles and squares) generally have negative slopes. For the retrograde patterns, the slopes are larger and more likely to be positive.

In Fig. 12, the observational data follow the general trend expected from theory but there is a large spread, which is due to the intrinsic glitches and dips in the period-spacing patterns. To include the deviations from the linear model, we used the residuals rather than the frequency uncertainties to estimate the uncertainty of slope. This process includes the uncertainty caused by the small glitches. However, there is another contribution to the slope uncertainty that comes from partially observed dips in the pattern. Fig. 13 shows the theoretical fit of KIC 4919344, where the measured slopes are significantly smaller than theory predicts. This systematic discrepancy is caused by broad dips in the period-spacing pattern that affect many radial orders, more, in fact, than are observable in this star. Another explanation for the discrepancy is that the global parameters of our sample ($\log g$, $T_{\rm eff}$, and metallicity) are not in the regime that was used by Ouazzani et al. (2017) to estimate the error margins (shaded area in Fig. 12).

6 CONCLUSIONS

Gravity-mode pulsations of γ Dor stars act as the probe of the stellar interior. The patterns showing equally spaced periods are distorted due to the molecular weight gradient and fast rotation. The dips, varying period spacings, as well as the missing peaks allow us to understand the physics of rotation and angular momentum transport in main-sequence stars and can place much-needed constraints

on diffusive mixing and chemical gradients, whilst also providing stellar ages.

In this paper, we tried two methods to parametrize the patterns. First, the 'moving-window FT' was used to detect the local periodicity in the period spectrum. It was partly successful since it can only give rough information about the period-spacing pattern. Secondly, the 'cross-correlation' optimizes the match between an artificial template and the observed spectrum. It can give the posterior distribution of the period, period spacing, and slope of a detected spacing pattern. We mainly used the second method to detect g-mode patterns.

To build a relation between the slope and the rotational rate, we applied our algorithm to 22 stars with observational rotational splitting. However, the splittings generally have the same magnitude as the period spacings, hence their patterns overlap and are hard to distinguish. We used the échelle diagram and the 'copy-shift' diagram to clarify their patterns and splittings and reported the first slope-vs-splitting diagram containing 22 slowly rotating targets. The observational evidence follows the theory that the slope deviates from zero when the splitting and hence the rotation rate increases. We also investigated the splitting variations for these stars. They show that for dipole modes the splitting typically rises or remains unchanged when the frequency increases. There are two stars whose apparent splittings and slopes are incompatible. These are explained by binaries with two similar period-spacing patterns from almost identical components.

ACKNOWLEDGEMENTS

We gratefully acknowledge support from the Australian Research Council, and from the Danish National Research Foundation (Grant DNRF106) through its funding for the Stellar Astrophysics Centre (SAC). We also thank the referee for very helpful comments.

REFERENCES

Aerts C., Christensen-Dalsgaard J., Kurtz D. W., 2010, Asteroseismology. Springer-Verlag, Berlin
Baglin A. et al., 2006, in COSPAR Meeting, 36th COSPAR Scientific Assembly, Beijing, China, p. 3749
Ballot J., Lignières F., Reese D. R., Rieutord M., 2010, A&A, 518, A30
Balona L. A., 2018, MNRAS, 475, 359
Balona L. A., Krisciunas K., Cousins A. W. J., 1994, MNRAS, 270, 905
Bedding T. R., 2014, Asteroseismology, 60, 6
Bedding T. R., Murphy S. J., Colman I. L., Kurtz D. W., 2015, EPJ Web. Conf., 101, 01005
Borucki W. J. et al., 2010, Science, 327, 977
Bouabid M.-P., Montalbán J., Miglio A., Dupret M.-A., Grigahcène A., Noels A., 2011, A&A, 531, A145
Bouabid M.-P., Dupret M.-A., Salmon S., Montalbán J., Miglio A., Noels A., 2013, MNRAS, 429, 2500
Breger M. et al., 1993, A&A, 271, 482
Chadid M., De Ridder J., Aerts C., Mathias P., 2001, A&A, 375, 113
Chapellier E., Mathias P., Weiss W. W., Le Contel D., Debosscher J., 2012, A&A, 540, A117
Christophe S., Ballot J., Ouazzani R.-M., Antoci V., Salmon S. J. A. J., 2018, A&A, 618, A47
Dupret M.-A., Grigahcène A., Garrido R., Gabriel M., Scuflaire R., 2004, A&A, 414, L17
Dupret M.-A., Grigahcène A., Garrido R., Gabriel M., Scuflaire R., 2005, A&A, 435, 927
Foreman-Mackey D., Hogg D. W., Lang D., Goodman J., 2013, PASP, 125, 306
Fukuda I., 1982, PASP, 94, 271
Giri S. K., Mellema G., Ghara R., 2018, MNRAS, 479, 5596
Groot P. J., Piters A. J. M., van Paradijs J., 1996, A&AS, 118, 545
Guo Z., Gies D. R., Matson R. A., 2017, ApJ, 851, 39
Guzik J. A., Kaye A. B., Bradley P. A., Cox A. N., Neuforge C., 2000, ApJ, 542, L57
Kaye A. B., Handler G., Krisciunas K., Poretti E., Zerbi F. M., 1999, PASP, 111, 840
Keen M. A., Bedding T. R., Murphy S. J., Schmid V. S., Aerts C., Tkachenko A., Ouazzani R.-M., Kurtz D. W., 2015, MNRAS, 454, 1792
Kjeldsen H., 2003, Ap&SS, 284, 1
Kjeldsen H., Bedding T. R., Viskum M., Frandsen S., 1995, AJ, 109, 1313
Kurtz D. W., Saio H., Takata M., Shibahashi H., Murphy S. J., Sekii T., 2014, MNRAS, 444, 102
Kurtz D. W., Shibahashi H., Murphy S. J., Bedding T. R., Bowman D. M., 2015, MNRAS, 450, 3015
Lampens P. et al., 2018, A&A, 610, A17
Ledoux P., 1951, ApJ, 114, 373
Lee U., Saio H., 1987, MNRAS, 224, 513
MacQueen J., 1967, in Le Cam L. M., Neyman J., eds, some Methods for Classification and Analysis of Multivariate Observations. Proceedings of the Fifth Berkeley Symposium on Mathematical Statistics and Probability, Volume 1: Statistics. Univ. California Press, Berkeley, p. 281
Miglio A., Montalbán J., Noels A., Eggenberger P., 2008, MNRAS, 386, 1487
Montgomery M. H., Odonoghue D., 1999, Delta Scuti Star Newsletter, 13, 28
Murphy S. J., Fossati L., Bedding T. R., Bedding T. R., Saio H., Kurtz D. W., Grassitelli L., Wang E. S., 2016a, MNRAS, 459, 1201
Murphy S. J., Moe M., Kurtz D. W., Bedding T. R., Shibahashi H., Boffin H. M. J., 2018, MNRAS, 474, 4322
Ouazzani R.-M., Salmon S. J. A. J., Antoci V., Bedding T. R., Murphy S. J., Roxburgh I. W., 2017, MNRAS, 465, 2294
Ouazzani R.-M., Marques J. P., Goupil M., Christophe S., Antoci V., Salmon S. J. A. J., 2018, preprint (arXiv:1801.09228)
Pápics P. I., 2012, Astron. Nachr., 333, 1053
Pápics P. I., Tkachenko A., Aerts C., Van Reeth T., De Smedt K., Hillen M., Østensen R., Moravveji E., 2015, ApJ, 803, L25
Pápics P. I. et al., 2017, A&A, 598, A74
Prat V., Mathis S., Lignières F., Ballot J., Culpin P.-M., 2017, A&A, 598, A105
Rahmani S., Teimoorinia H., Barmby P., 2018, MNRAS, 478, 4416
Reed M. D. et al., 2011, MNRAS, 414, 2885
Royer F., Zorec J., Gómez A. E., 2007, A&A, 463, 671
Saio H., 1981, ApJ, 244, 299
Saio H., Kurtz D. W., Takata M., Shibahashi H., Murphy S. J., Sekii T., Bedding T. R., 2015, MNRAS, 447, 3264
Saio H., Kurtz D. W., Murphy S. J., Antoci V. L., Lee U., 2018a, MNRAS, 474, 2774
Saio H., Bedding T. R., Kurtz D. W., Murphy S. J., Antoci V., Shibahashi H., Li G., Takata M., 2018b, MNRAS, 477, 2183
Schmid V. S. et al., 2015, A&A, 584, A35
Shibahashi H., 1979, PASJ, 31, 87
Sowicka P., Handler G., Dębski B., Jones D., Van de Sande M., Pápics P. I., 2017, MNRAS, 467, 4663
Stumpe M. C., Smith J. C., Catanzarite J. H., Van Cleve J. E., Jenkins J. M., Twicken J. D., Girouard F. R., 2014, PASP, 126, 100
Su J., Li Y., Fu J.-N., Li C., 2014, MNRAS, 437, 2566
Tassoul M., 1980, ApJS, 43, 469
Townsend R. H. D., 2003, MNRAS, 340, 1020
Townsend R. H. D., Teitler S. A., 2013, MNRAS, 435, 3406
Van Reeth T. et al., 2015a, ApJS, 218, 27
Van Reeth T. et al., 2015b, A&A, 574, A17
Van Reeth T., Tkachenko A., Aerts C., 2016, A&A, 593, A120
Van Reeth T. et al., 2018, A&A, 618, A24
Wu J., 2010, Advances in K-means Clustering: A Data Mining Thinking. Springer, Berlin

APPENDIX A: RESULTS FOR 24 STARS

In the appendix, we display the amplitude spectra, the period spacing patterns, the échelle diagrams, and splitting variations for 24 multiplet stars. The splittings of KIC 6862920 and KIC 8458690 are just the binary effects, while other 22 stars show the rotational effects.

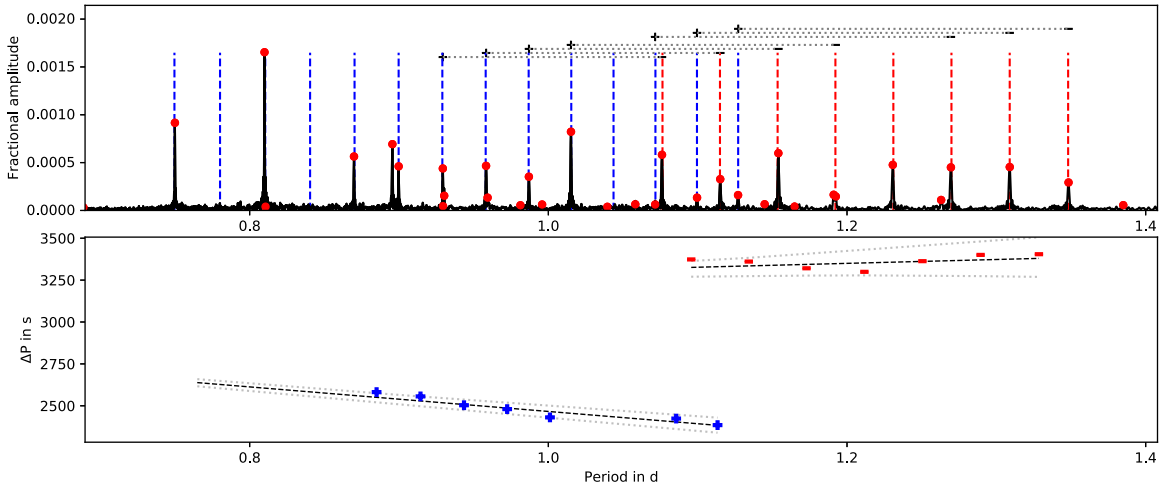

Figure A1. Rotationally split doublets in KIC 2450944. Upper panel: the period spectrum and doublets. The solid red circles show the independent frequencies, while open red circles are likely combination frequencies (none present in this figure). The vertical dashed lines mark the linear fit. The horizontal dashed lines show the splittings. The symbol '+' means $m = +1$. '-' denotes $m = -1$. 'o' will be used in other figures to show $m = 0$ modes. Lower panel: the period spacing patterns. The markers are the period spacings, using $(P_i + P_{i+1})/2$ as their x-coordinates. The black dashed lines show the linear fit while the grey dotted lines around them present the uncertainties. The blue pluses present $l = 1$, $m = 1$ modes. The red minuses are $l = 1$, $m = -1$ modes.

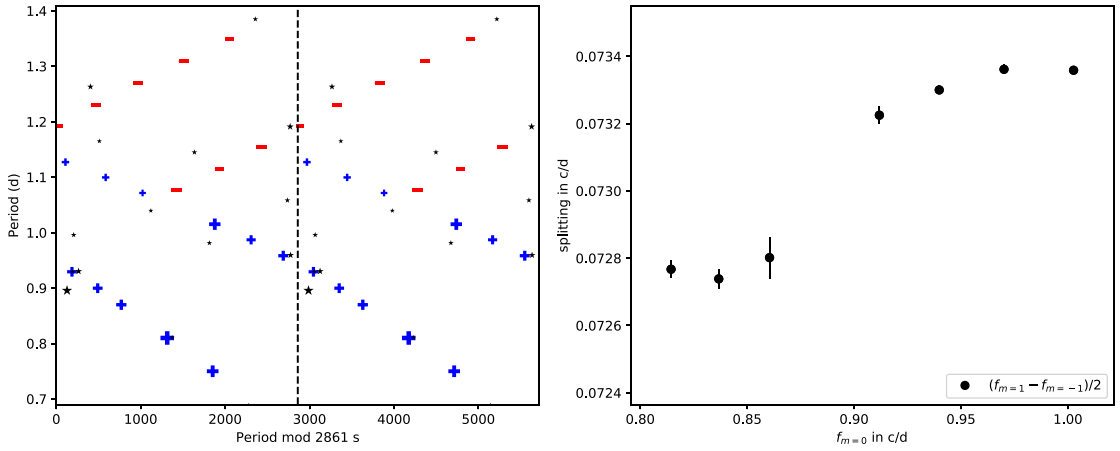

Figure A2. The échelle diagram and the splitting variations of KIC 2450944. Left-hand panel: the échelle diagram. Different symbols and colours represent different azimuzal orders, as in Fig. A1. The black crosses show the peaks that do not belong to any pattern. Right-hand panel: splitting variation with $m = 0$ frequency. The error bars show the frequency uncertainties calculated by equation (1).

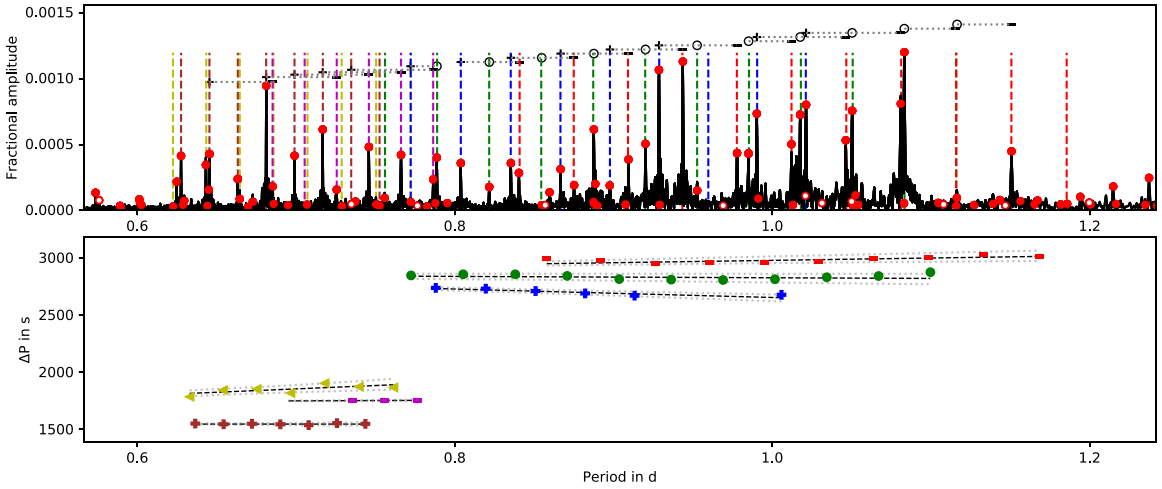

Figure A3. The period spacing patterns of KIC 3127996. The period spacing patterns of $l = 1$ and 2 modes are seen in the same time, shown in the second panel. The blue pluses show $l = 1$, $m = 1$ modes, the green circles show $l = 1$, $m = 0$ modes, the red minuses are $l = 1$, $m = -1$ modes, the brown pluses are $l = 2$, $m = 1$ modes, the purple minus are $l = 2$, $m = 1$ modes, and the yellow triangles represent $l = 2$, $m = -2$ modes.

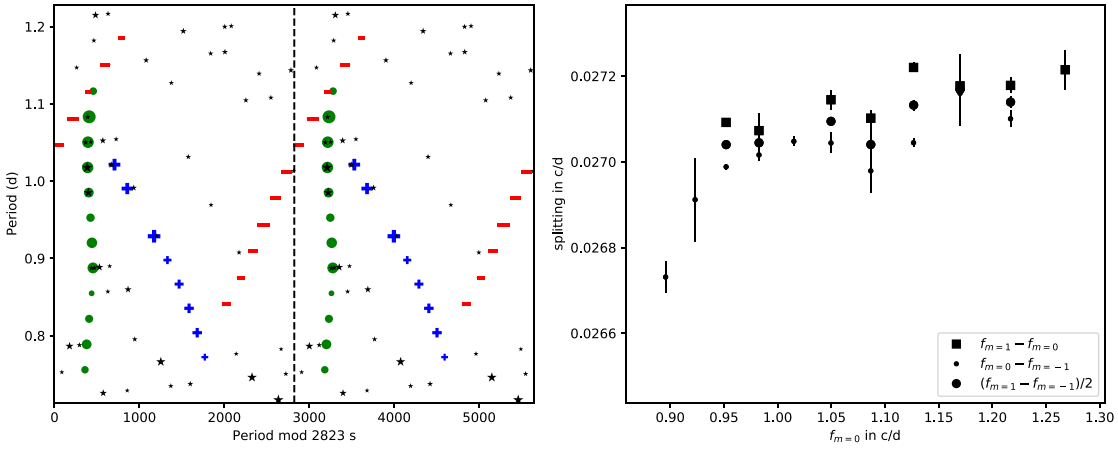

Figure A4. The échelle diagram and the splitting variations of $l = 1$ modes of KIC 3127996.

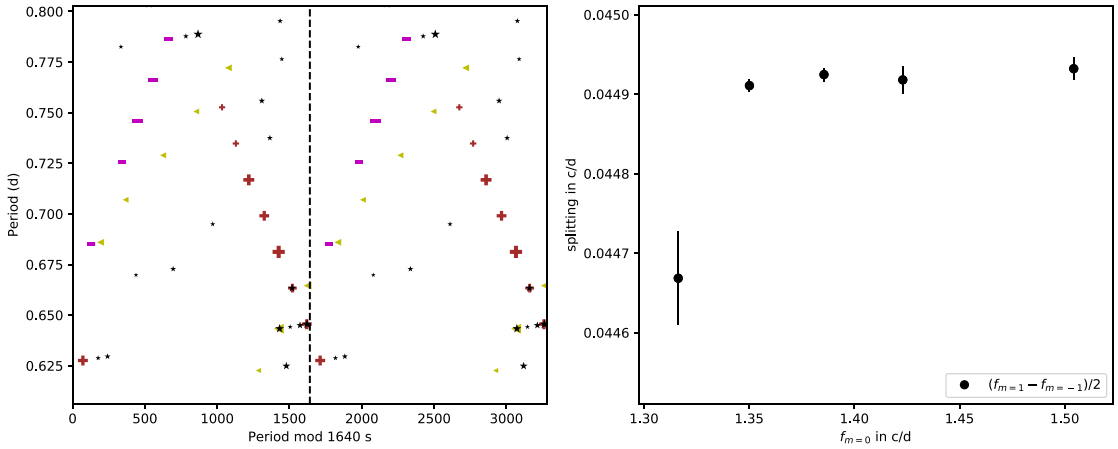

Figure A5. The échelle diagram and the splitting variations of $l = 2$ modes of KIC 3127996.

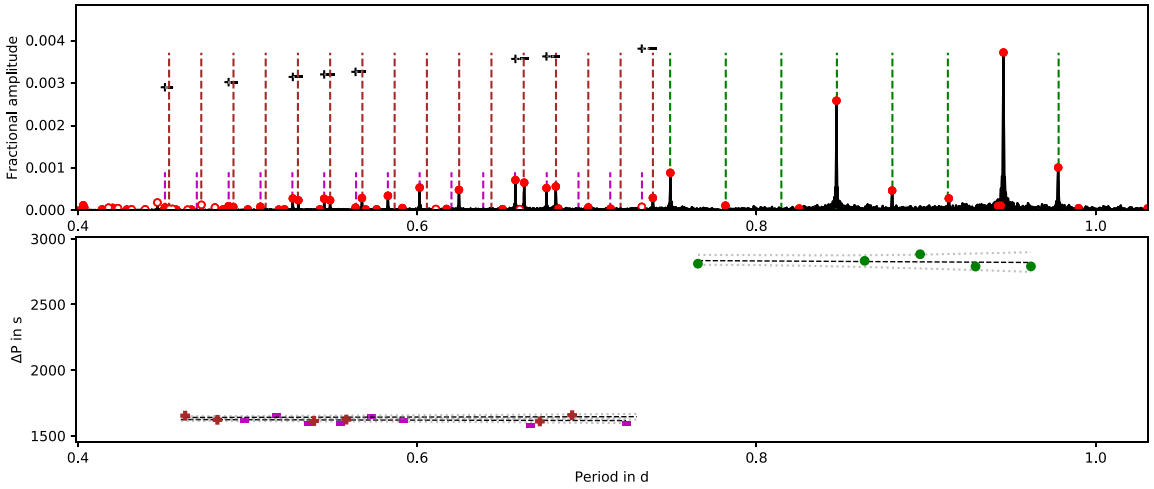

Figure A6. The period spacing patterns of KIC 3222854. Note that the splittings are $l = 2$ modes. The azimuthal orders for two $l = 2$ patterns cannot been determined. We assume they are $m = \pm 1$ modes.

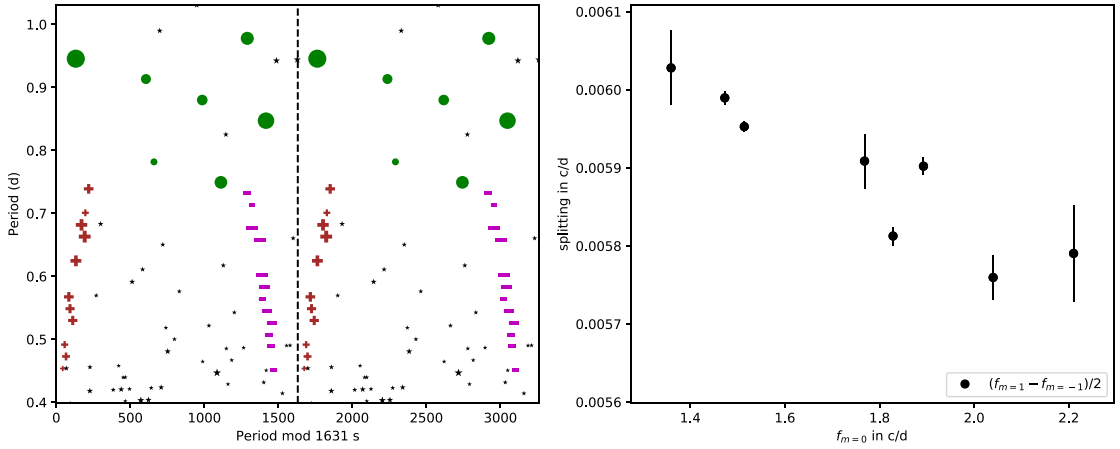

Figure A7. The échelle diagram and the splitting variations of KIC 3222854. Note that the splittings are $l = 2$ modes.

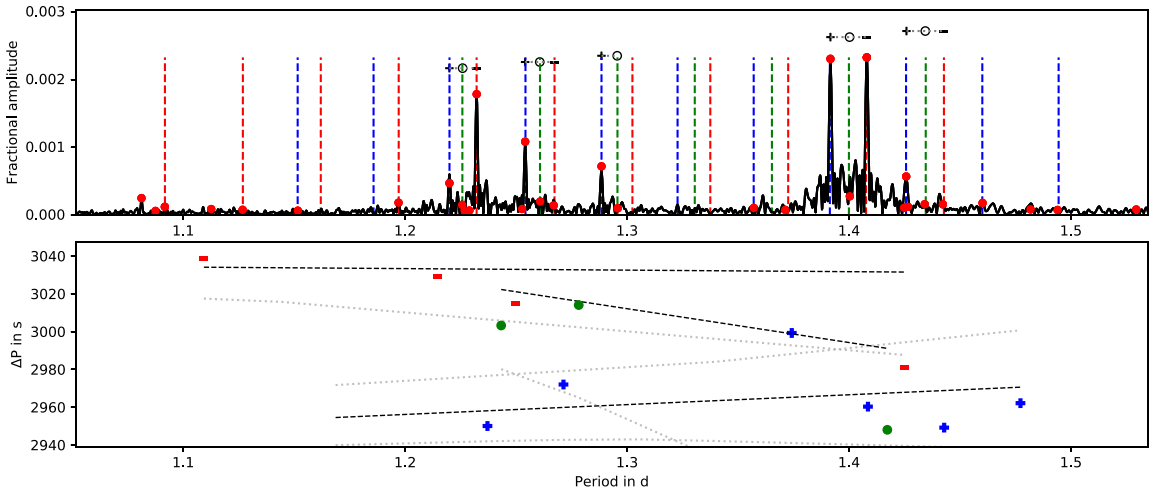

Figure A8. The period spacing patterns of KIC 4480321.

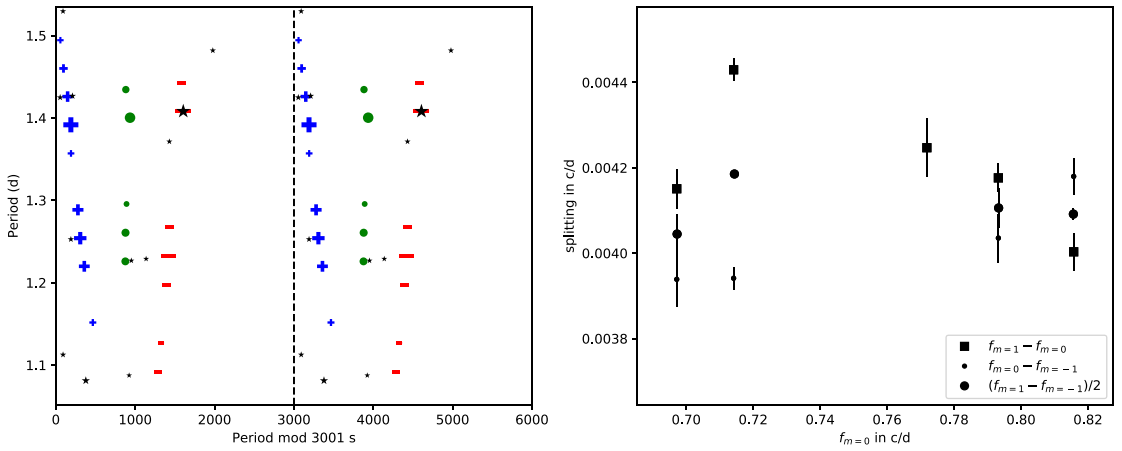

Figure A9. The echelle diagram and the splitting variations of KIC 4480321.

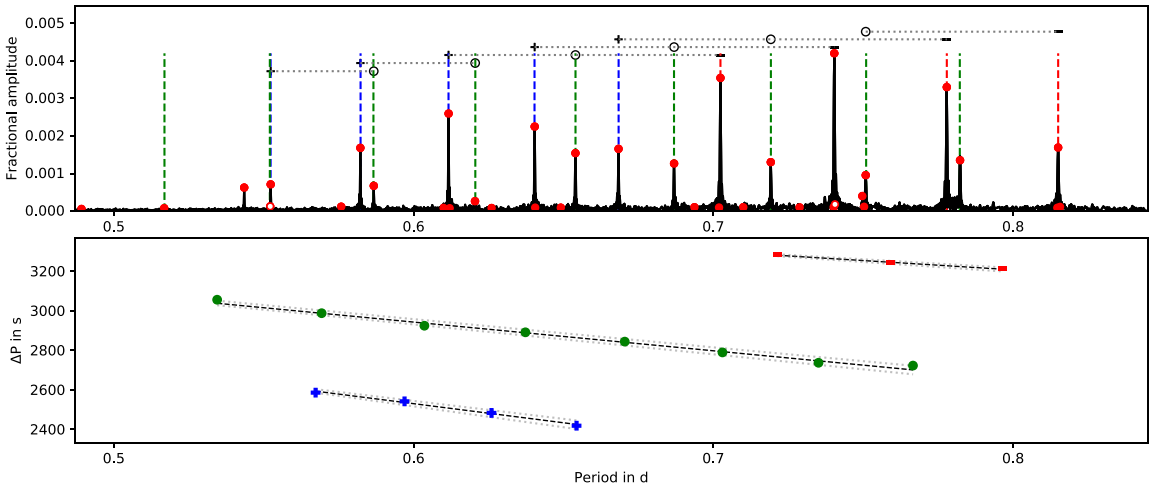

Figure A10. The period spacing patterns of KIC 4919344.

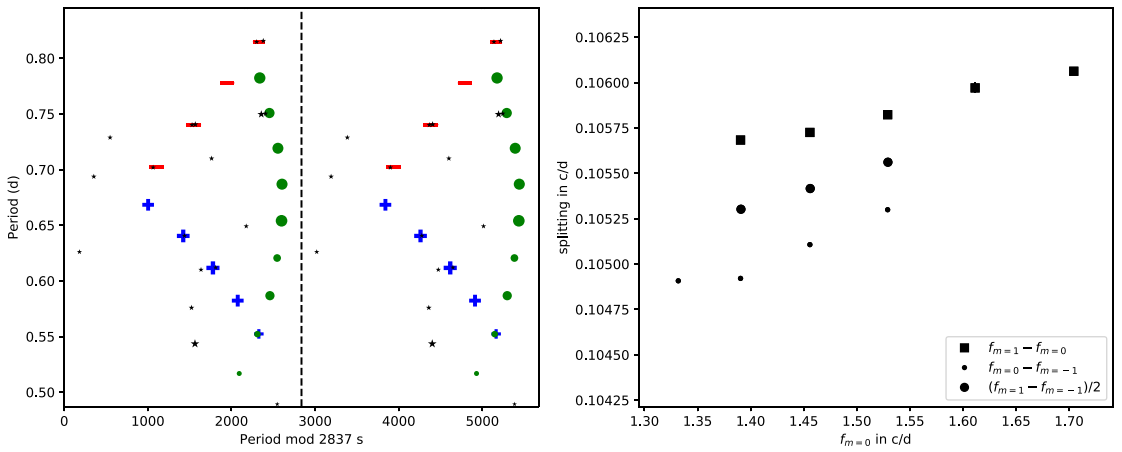

Figure A11. The échelle diagram and the splitting variations of KIC 4919344.

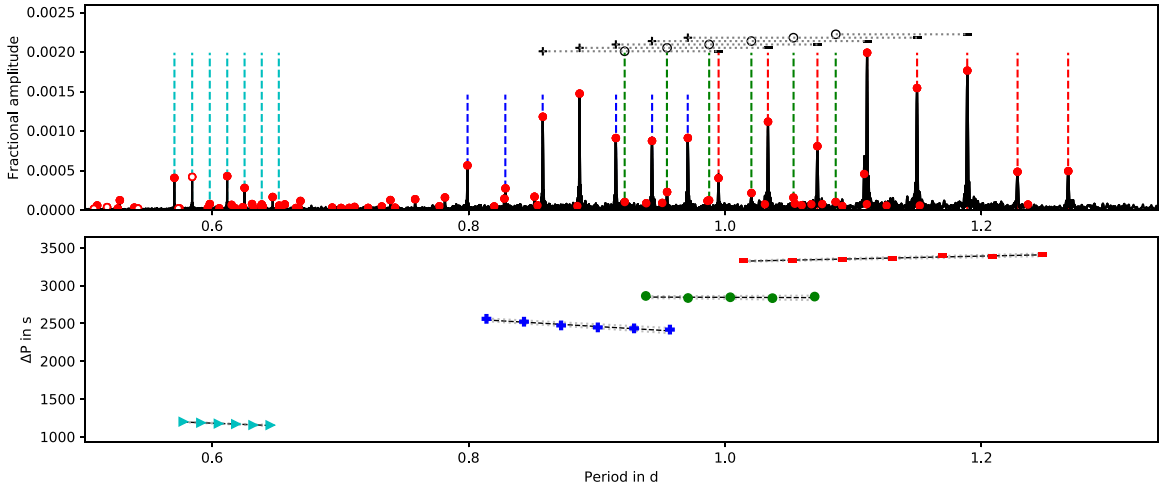

Figure A12. The period spacing patterns of KIC 5038228. $l = 2$, $m = 2$ patterns are seen, shown as cyan right triangles.

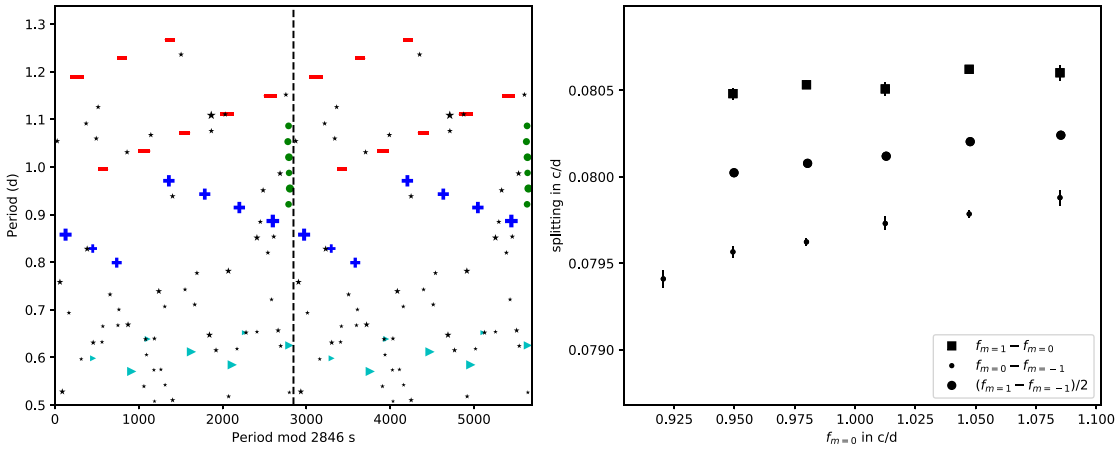

Figure A13. The échelle diagram and the splitting variations of KIC 5038228.

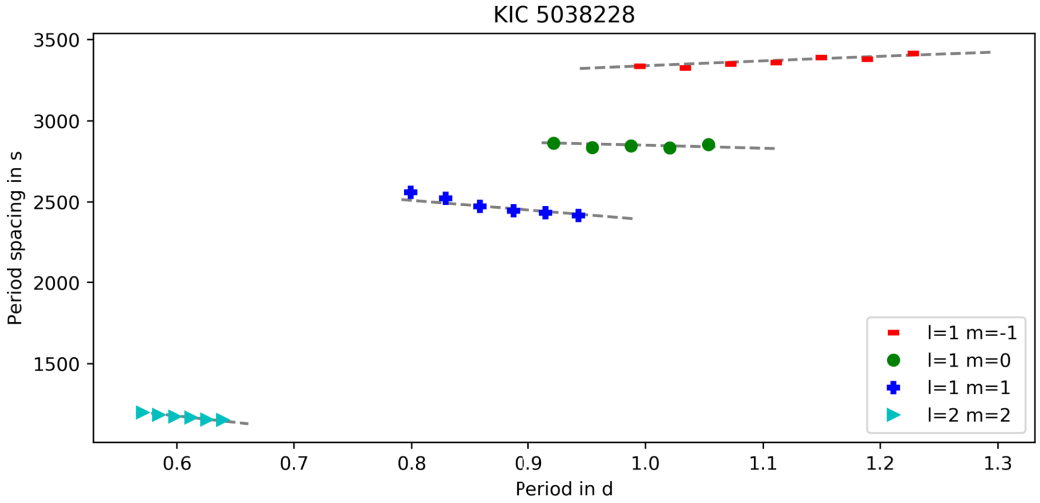

Figure A14. The modes identification of KIC 5038228 from the TAR.

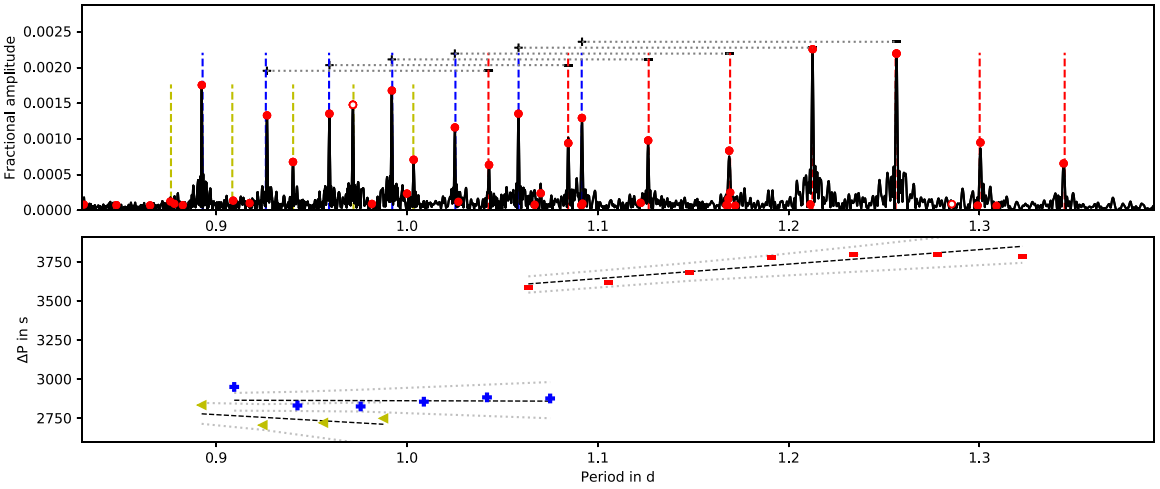

Figure A15. The period spacing patterns of KIC 5459805. Note that the splittings are not the effect of rotation.

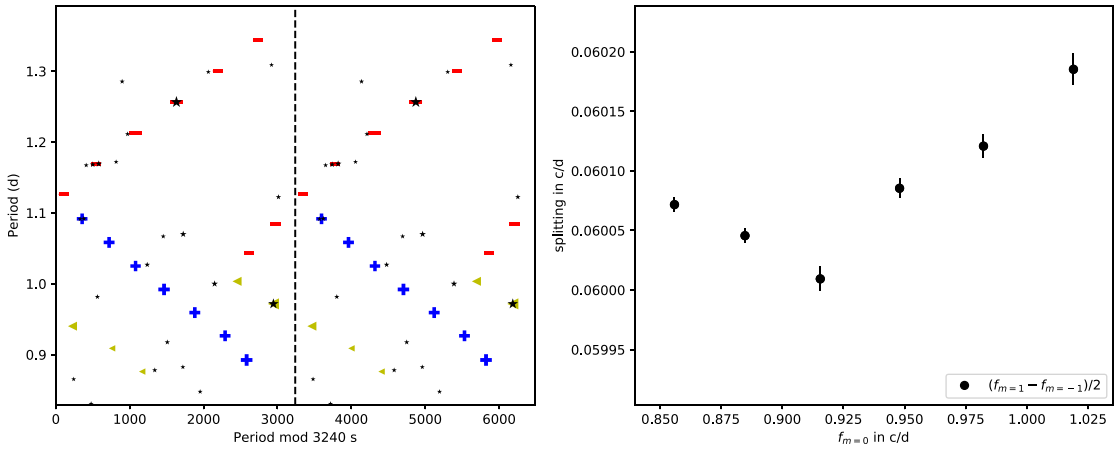

Figure A16. The échelle diagram and the splitting variations of KIC 5459805.

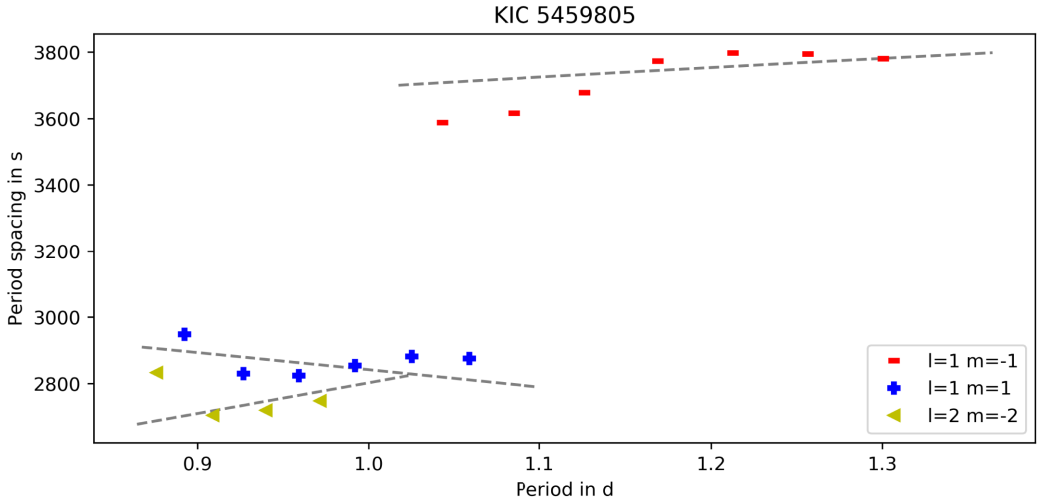

Figure A17. The modes identification of KIC 5459805.

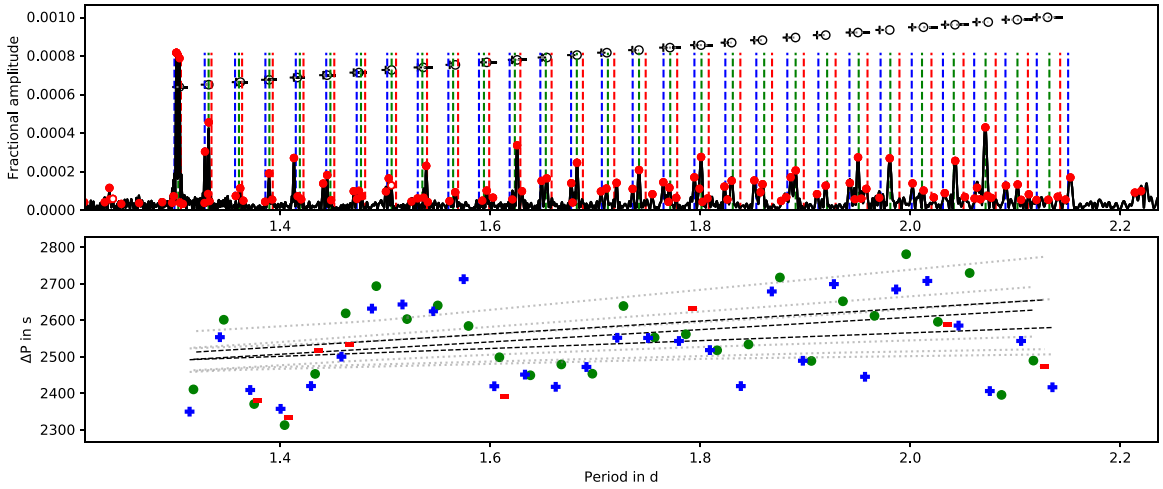

Figure A18. The period spacing patterns of KIC 5557072.

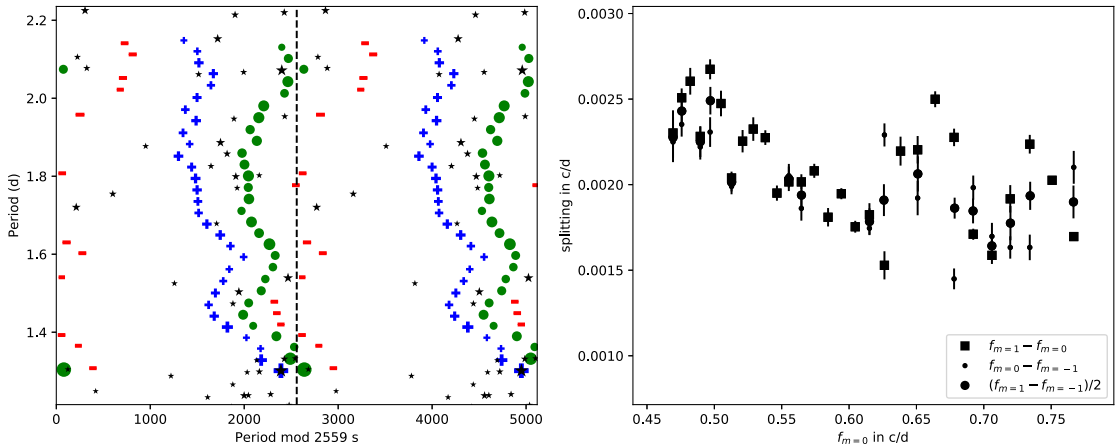

Figure A19. The échelle diagram and the splitting variations of KIC 5557072.

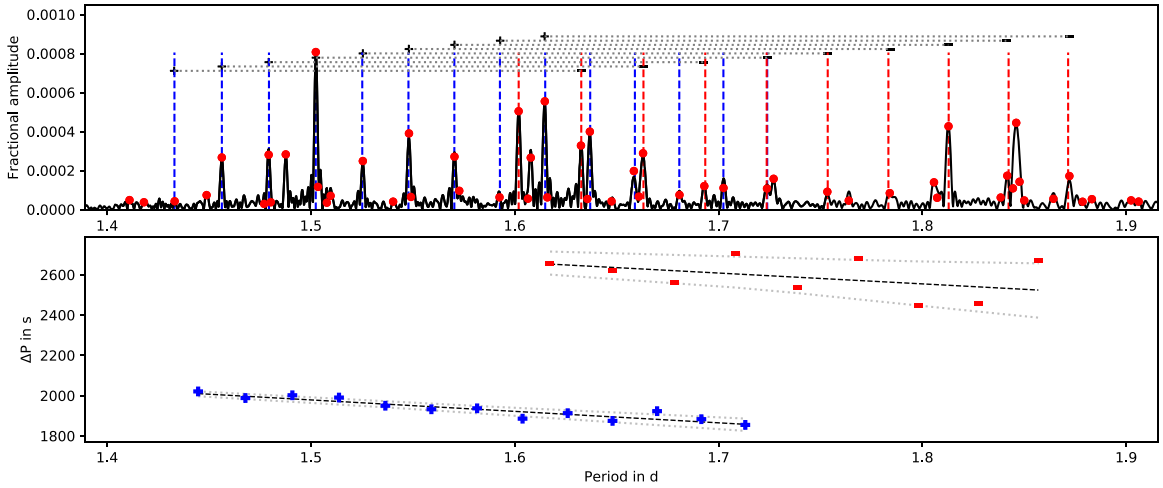

Figure A20. The period spacing patterns of KIC 5810197.

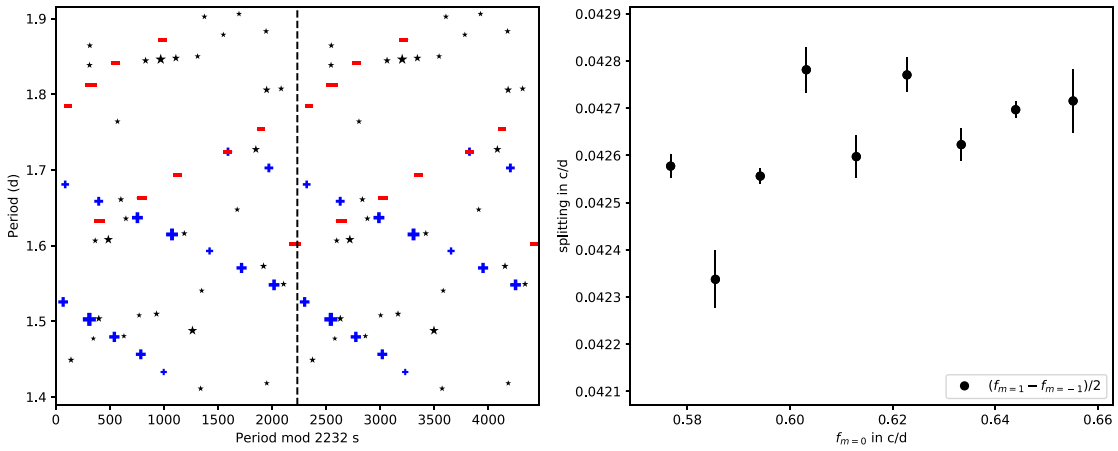

Figure A21. The échelle diagram and the splitting variations of KIC 5810197.

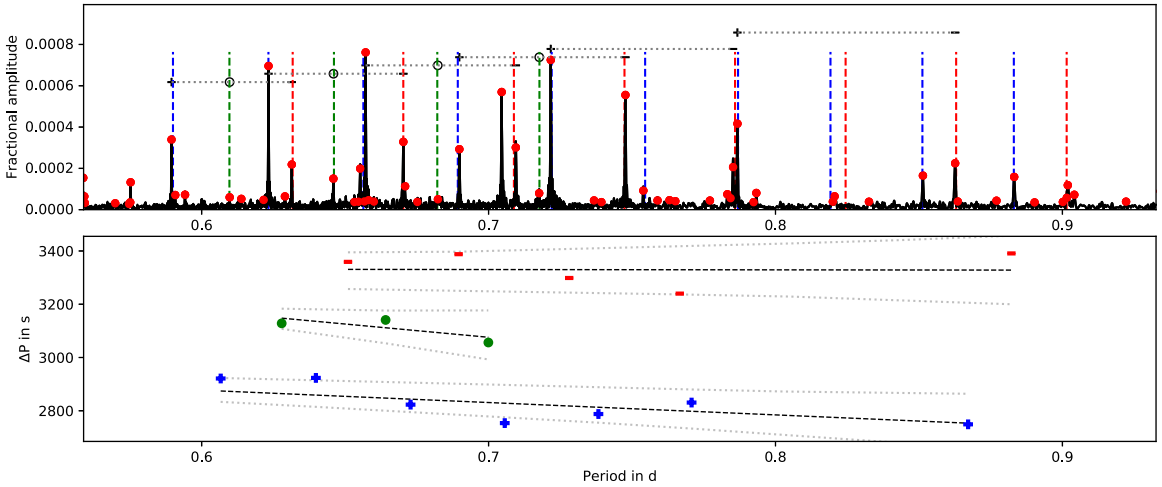

Figure A22. The period spacing patterns of KIC 6302589.

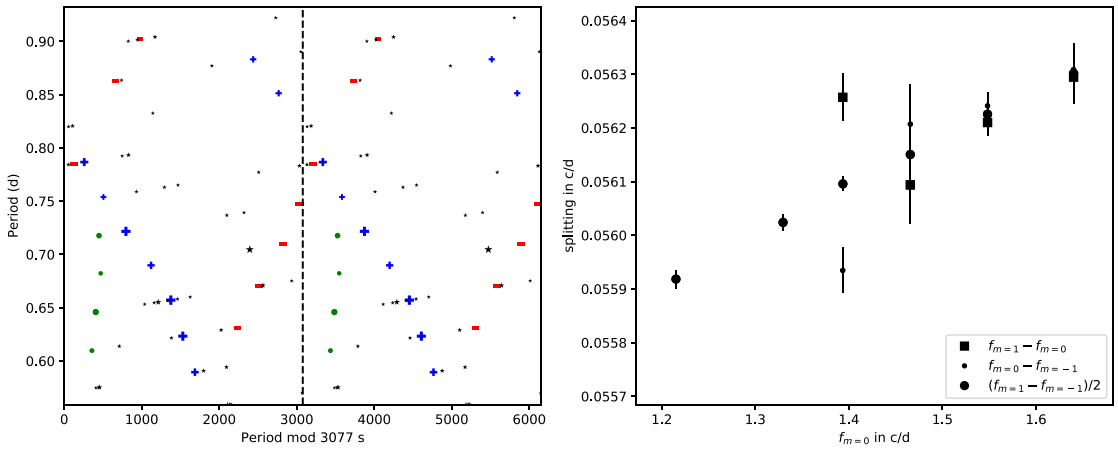

Figure A23. The échelle diagram and the splitting variations of KIC 6302589.

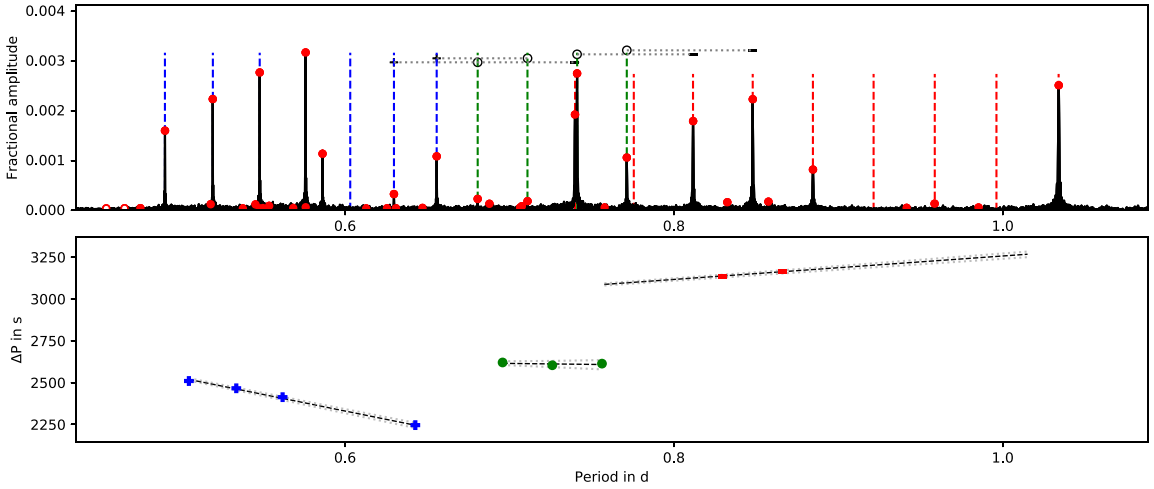

Figure A24. The period spacing patterns of KIC 6467639.

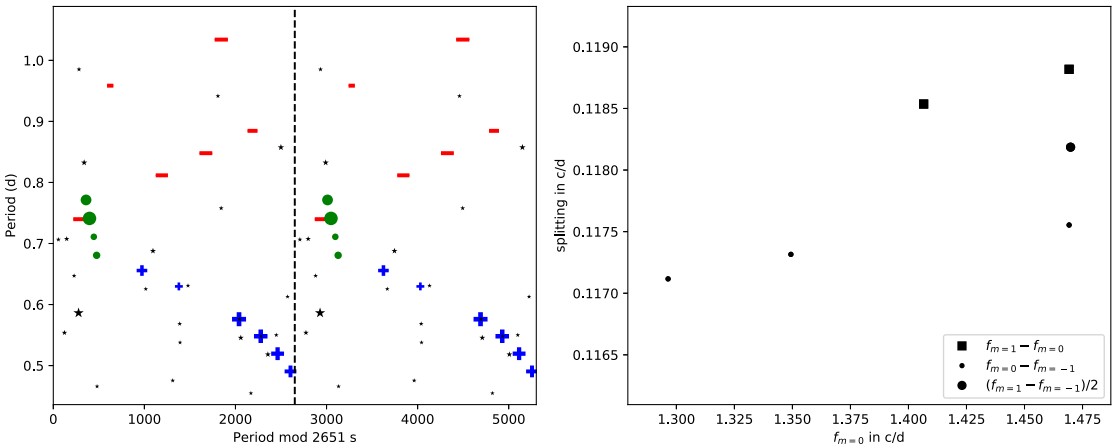

Figure A25. The échelle diagram and the splitting variations of KIC 6467639.

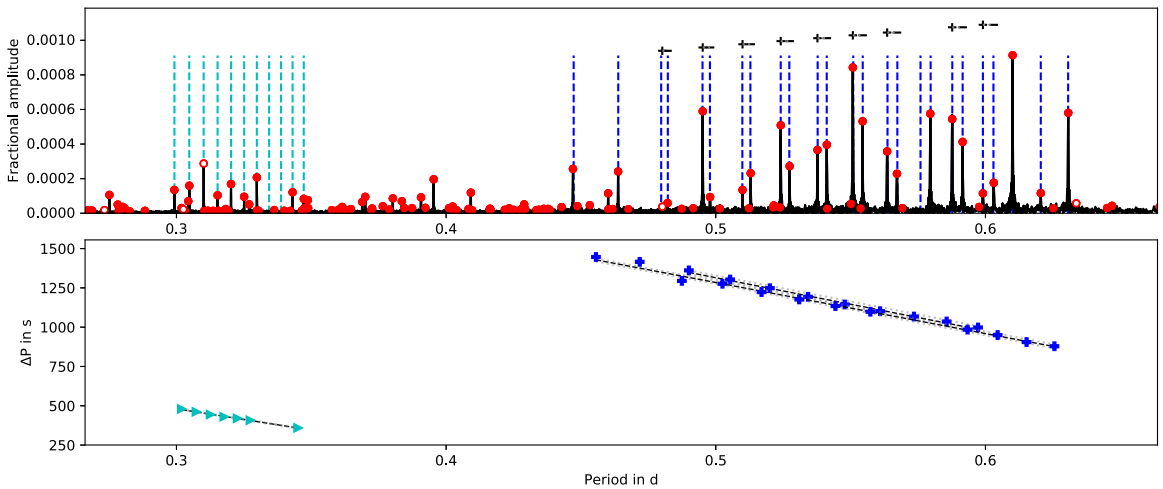

Figure A26. The period spacing patterns of KIC 6862920. Note that the splittings are not the effect of rotation.

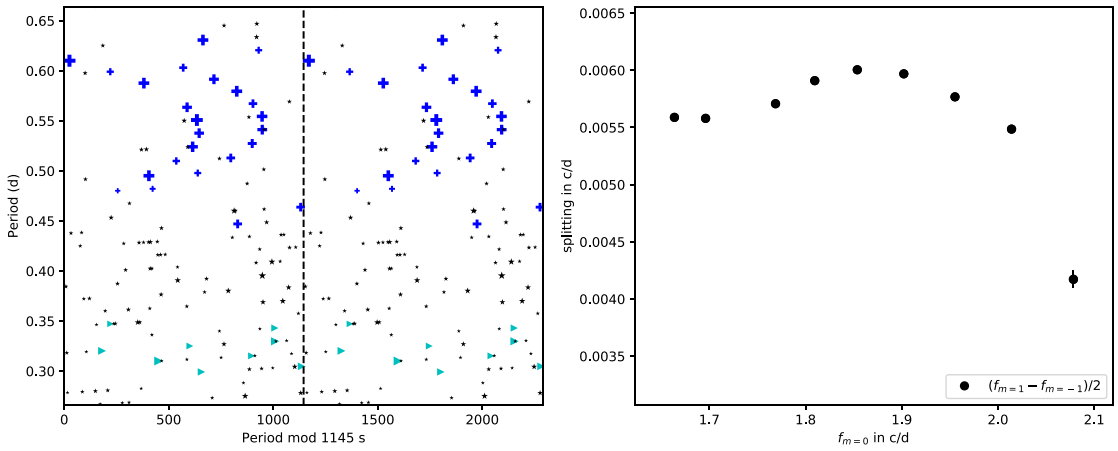

Figure A27. The échelle diagram and the splitting variations of KIC 6862920. Note that the splittings are not caused by the rotational effect.

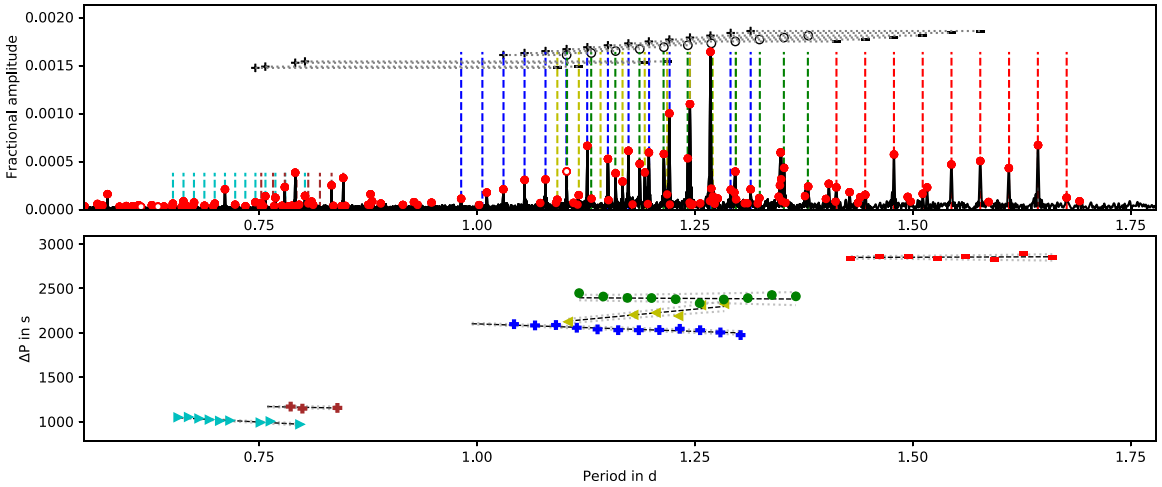

Figure A28. The period spacing patterns of KIC 6937123. Note that the splittings are not caused by the rotational effect.

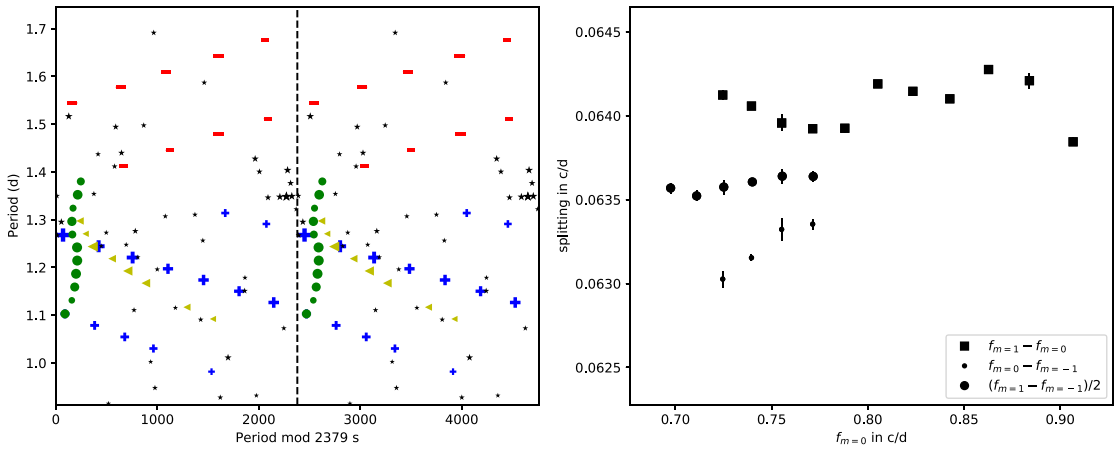

Figure A29. The échelle diagram and the splitting variations of KIC 6937123 of $l = 1$ modes.

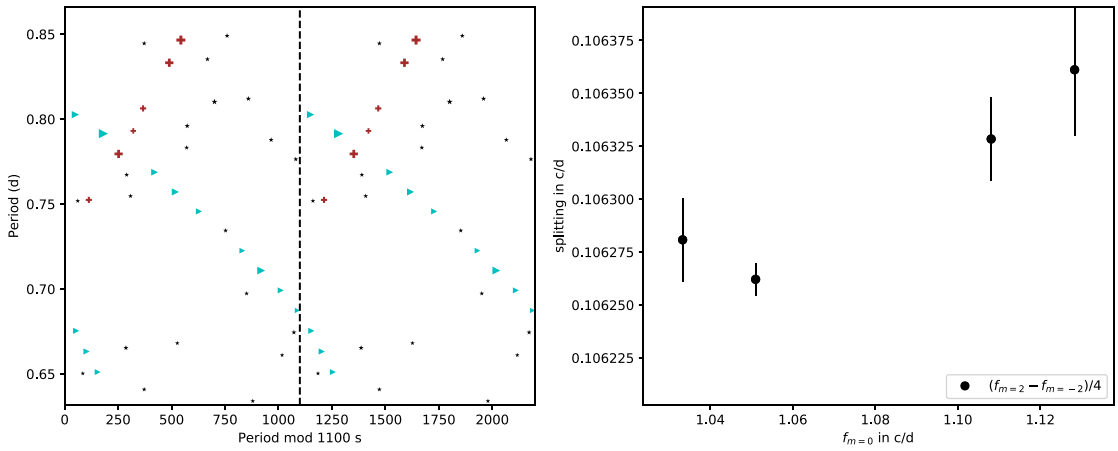

Figure A30. The échelle diagram and the splitting variations of KIC 6937123 of $l = 2$ modes.

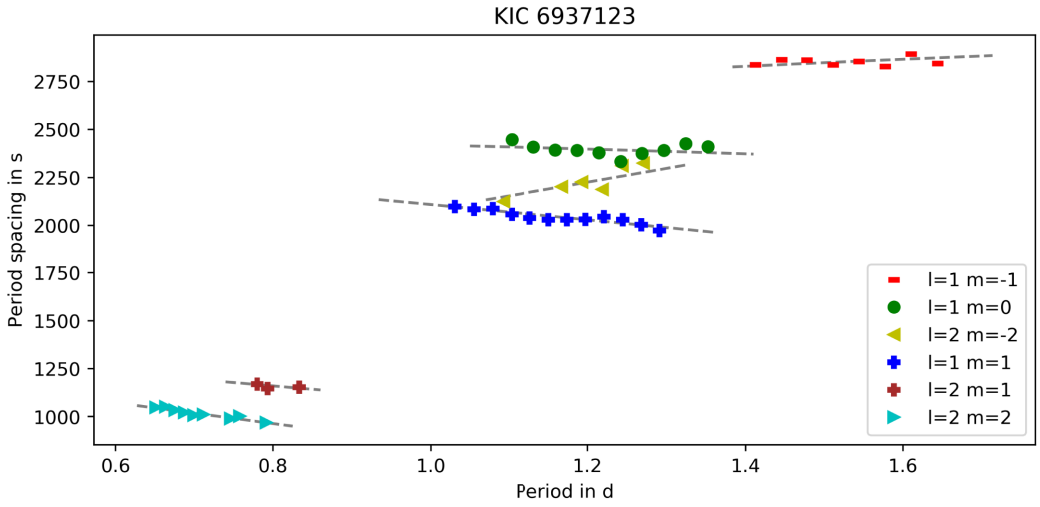

Figure A31. The modes identification of KIC 6937123.

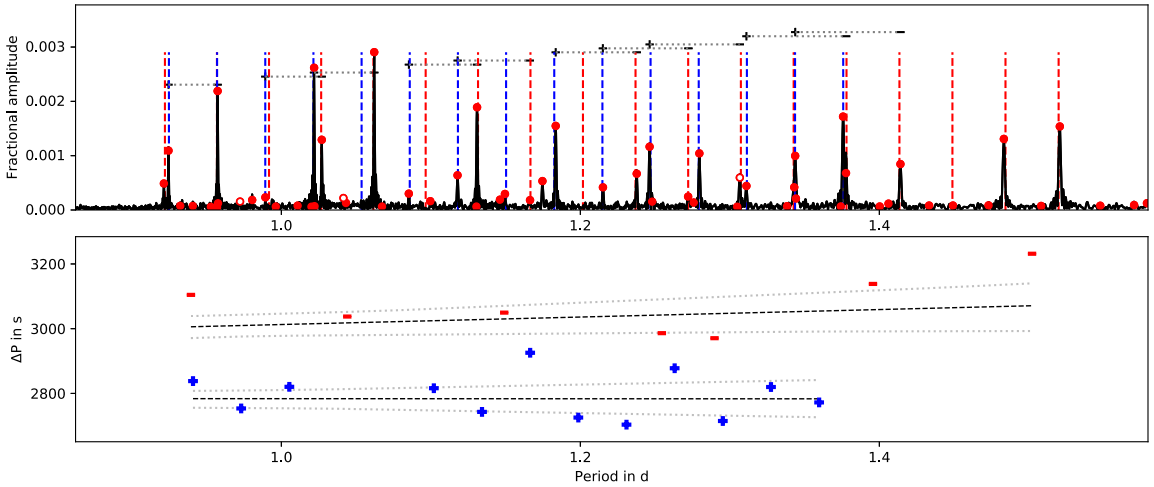

Figure A32. The period spacing patterns of KIC 7661054.

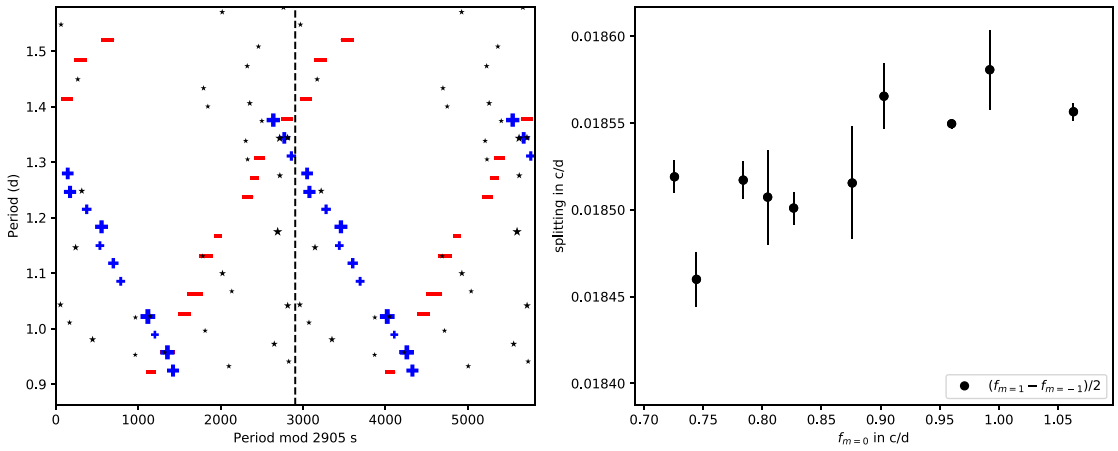

Figure A33. The échelle diagram and the splitting variations of KIC 7661054.

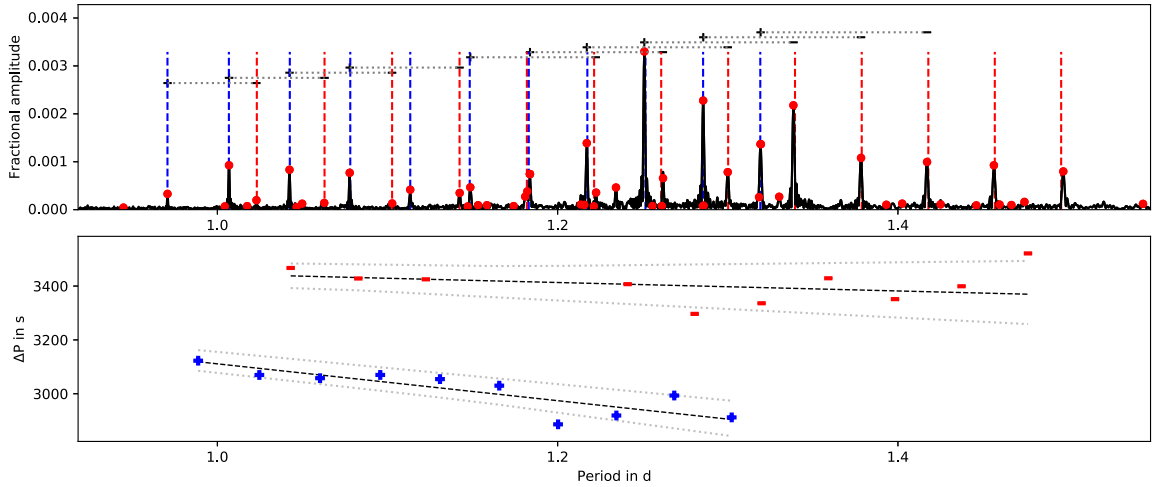

Figure A34. The period spacing patterns of KIC 7697861.

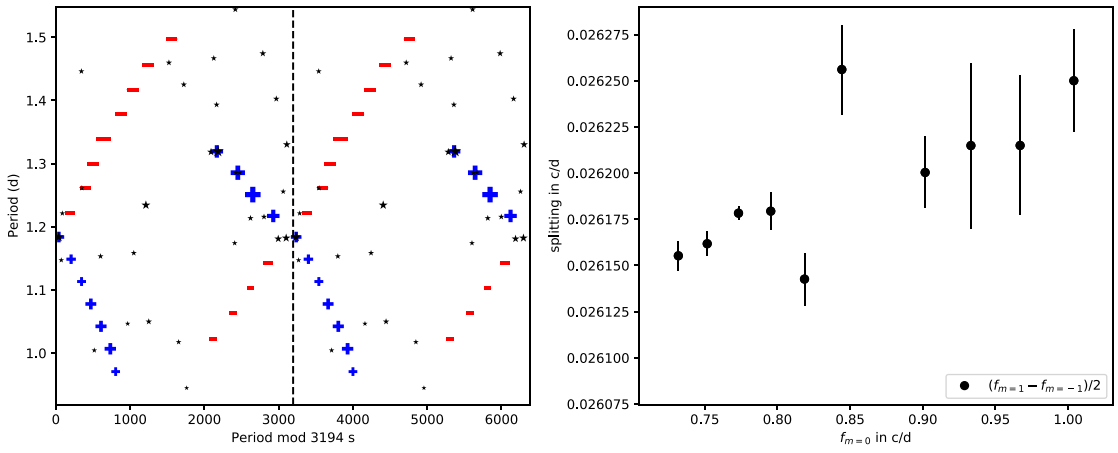

Figure A35. The échelle diagram and the splitting variations of KIC 7697861.

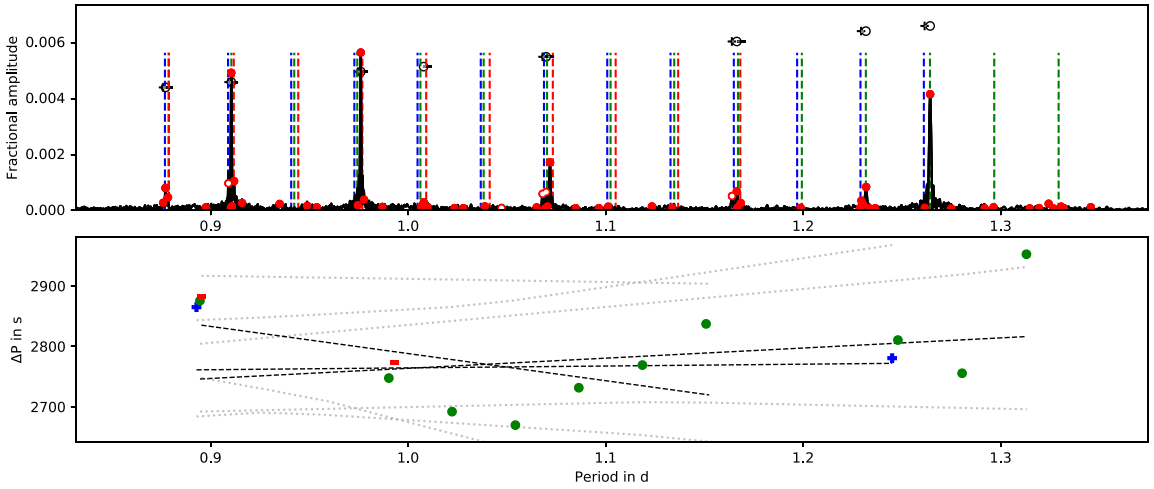

Figure A36. The period spacing patterns of KIC 8197761. Note the apparent dip shown in by the red circles.

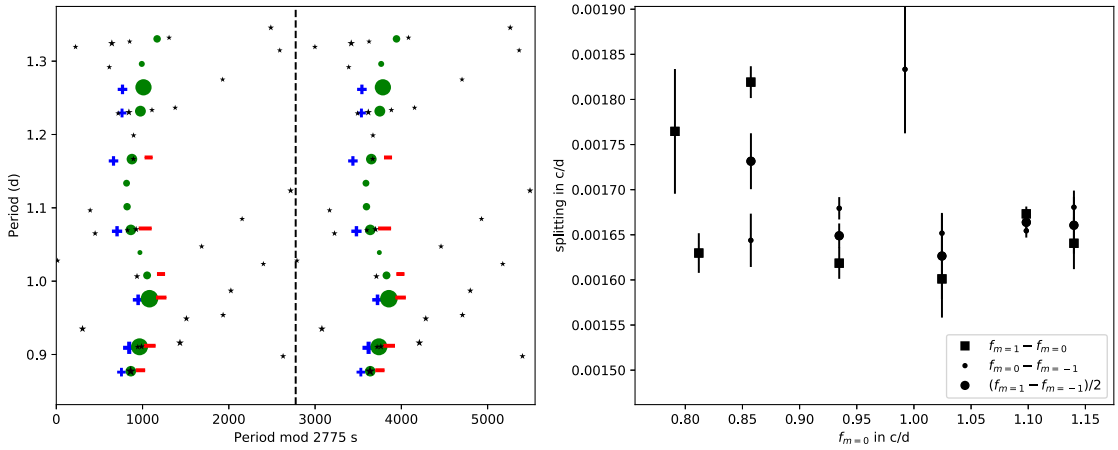

Figure A37. The echelle diagram and the splitting variations of KIC 8197761.

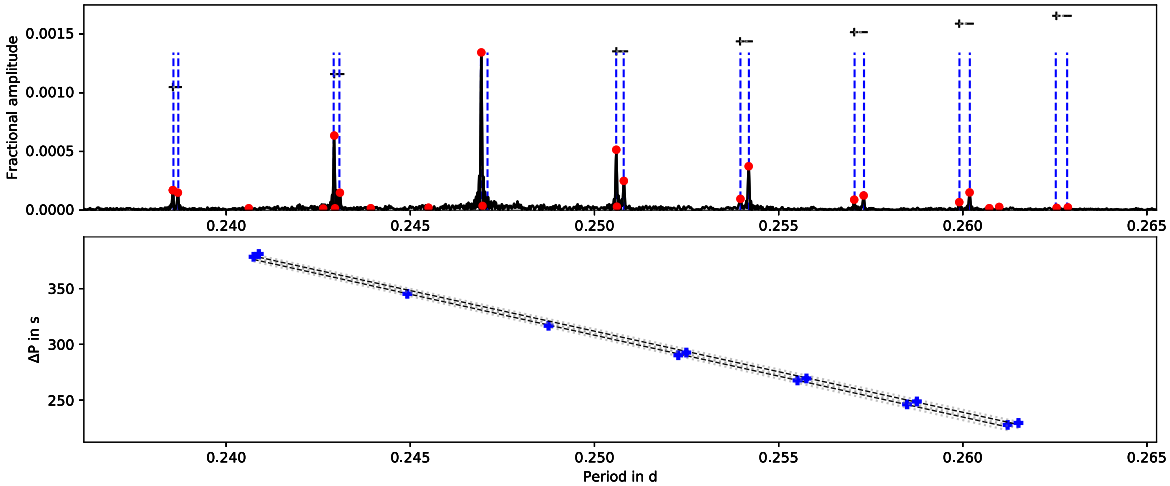

Figure A38. The period spacing patterns of KIC 8458690. Note that the splittings are not caused by the rotational effect.

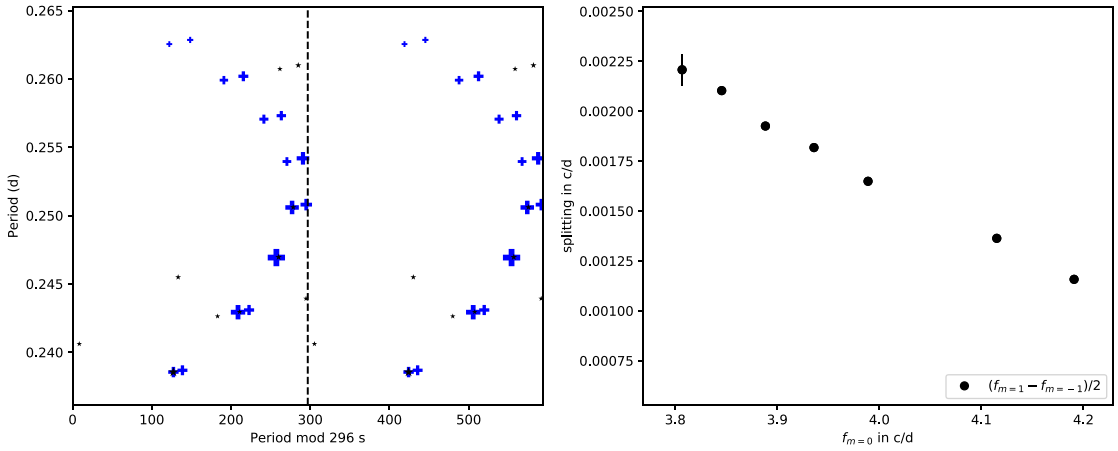

Figure A39. The échelle diagram and the splitting variations of KIC 8458690. Note that the splittings are not caused by the rotational effect.

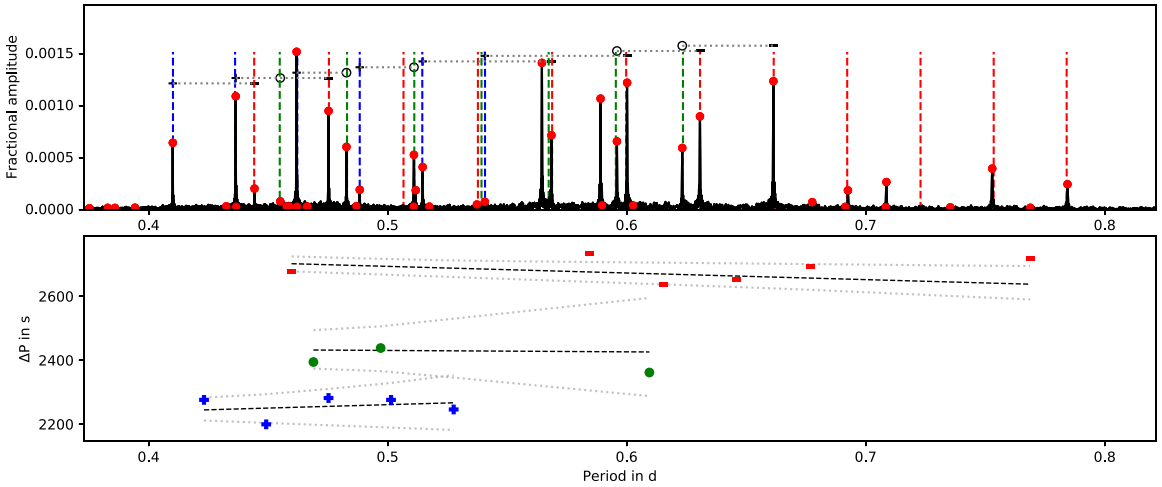

Figure A40. The period spacing patterns of KIC 9028134.

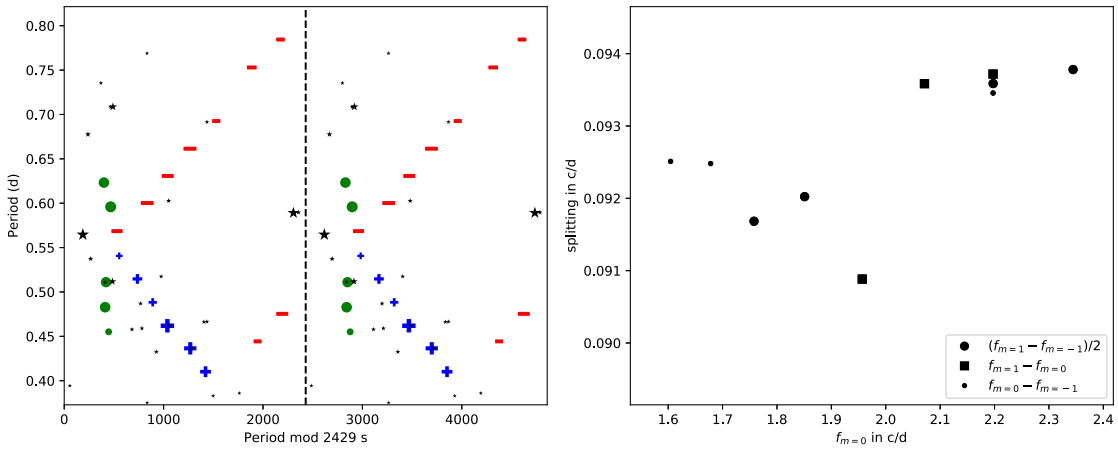

Figure A41. The échelle diagram and the splitting variations of KIC 9028134.

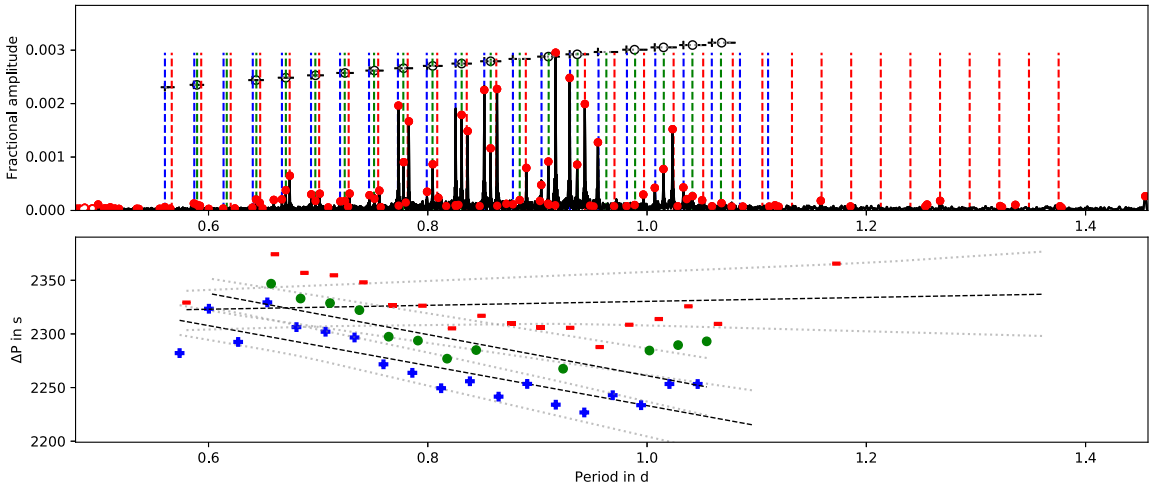

Figure A42. The period spacing patterns of KIC 9244992.

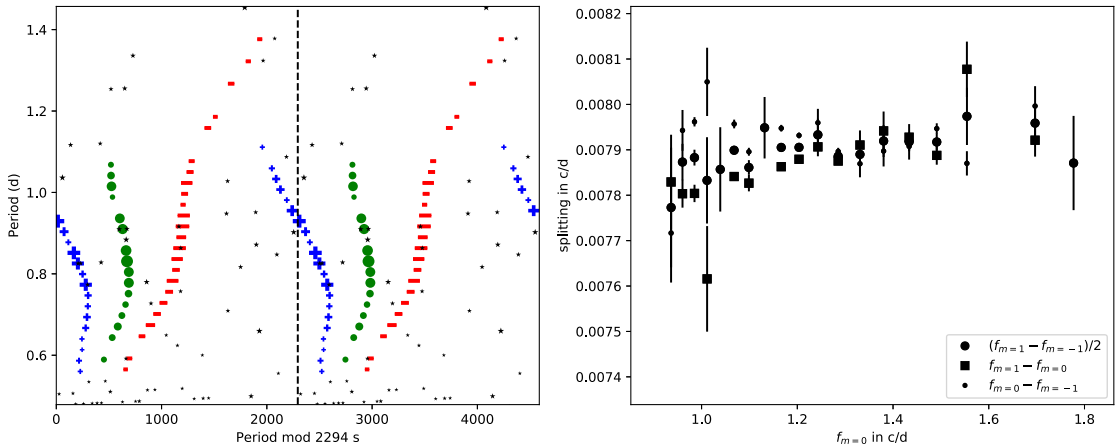

Figure A43. The échelle diagram and the splitting variations of KIC 9244992.

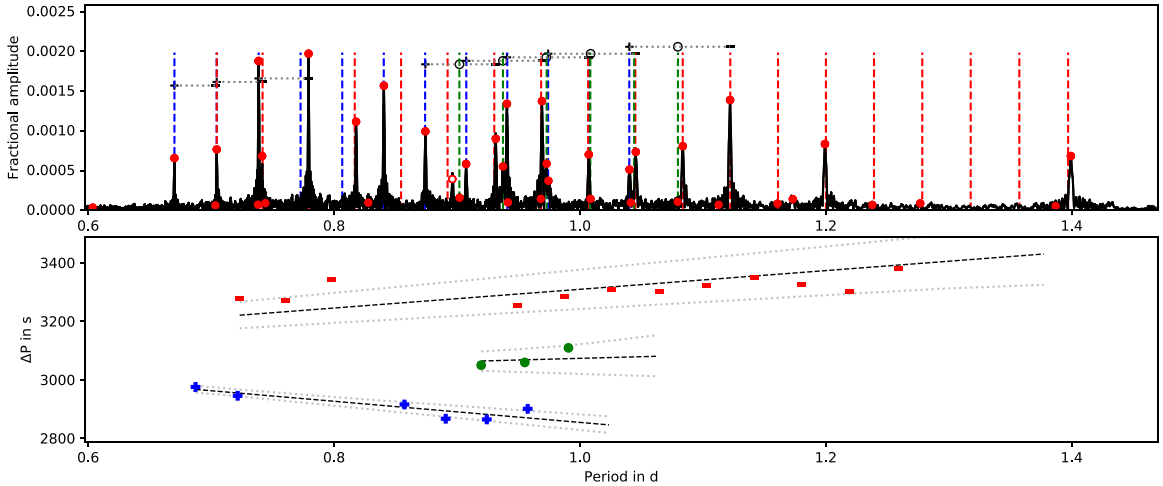

Figure A44. The period spacing patterns of KIC 9751996.

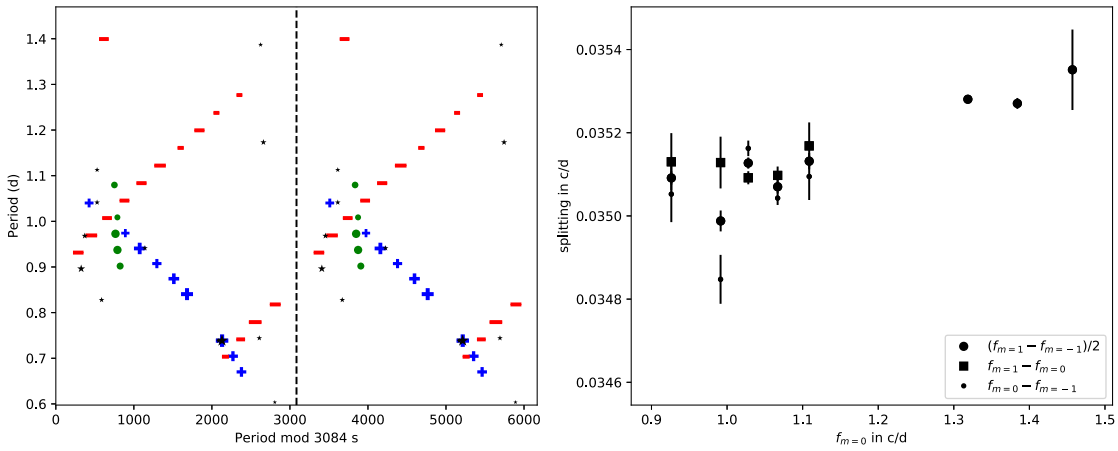

Figure A45. The échelle diagram and the splitting variations of KIC 9751996.

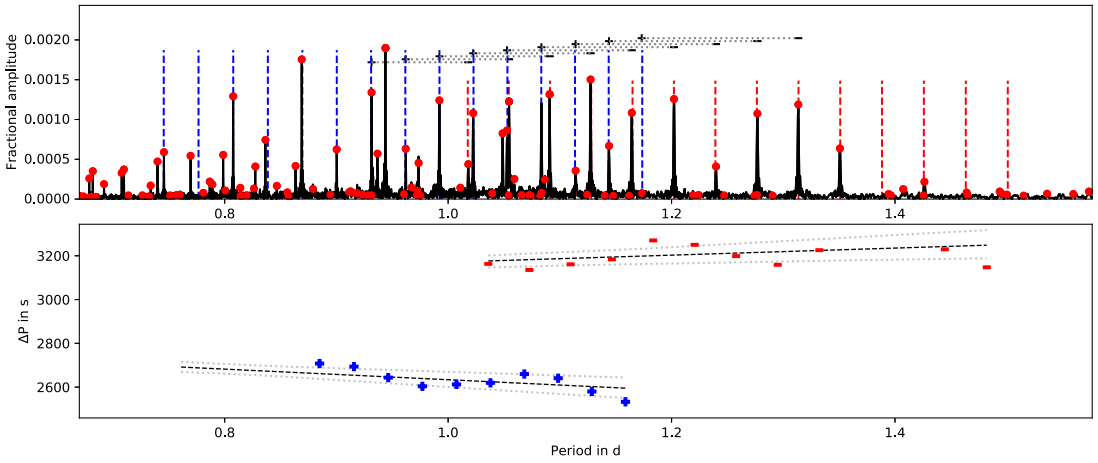

Figure A46. The period spacing patterns of KIC 10080943(B).

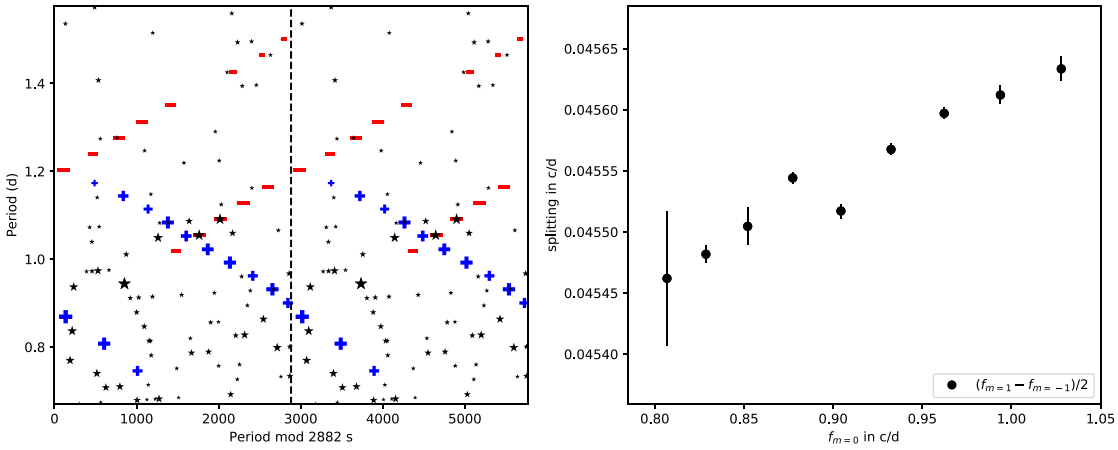

Figure A47. The échelle diagram and the splitting variations of KIC 10080943(A).

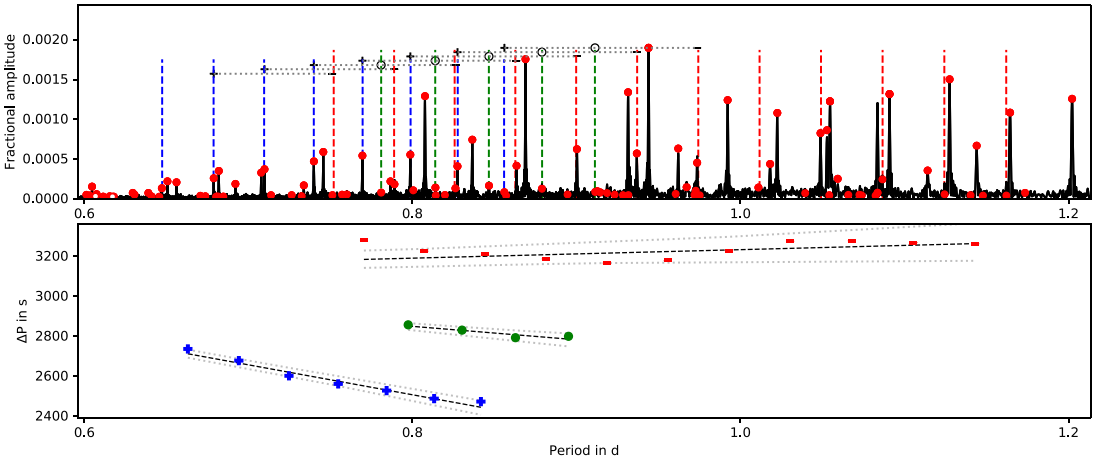

Figure A48. The period spacing patterns of KIC 10080943(B).

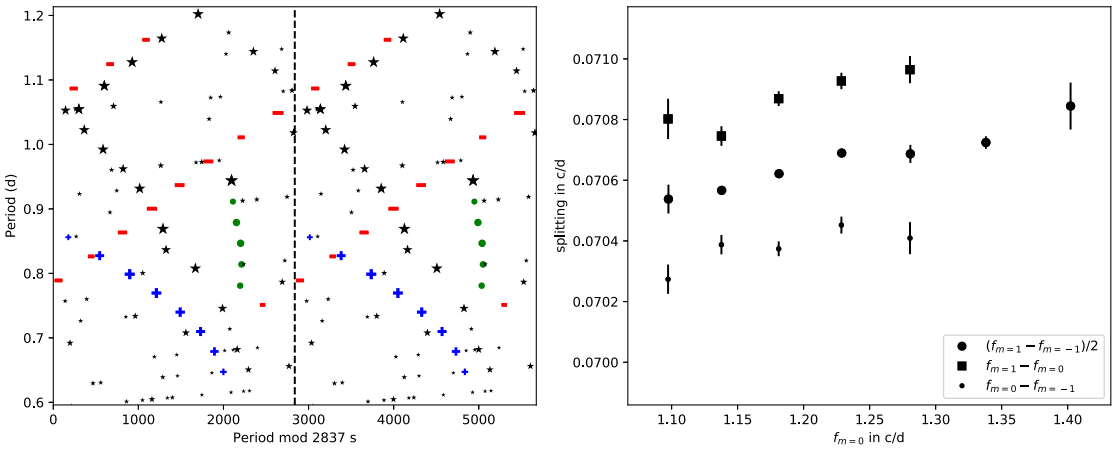

Figure A49. The échelle diagram and the splitting variations of KIC 10080943(B).

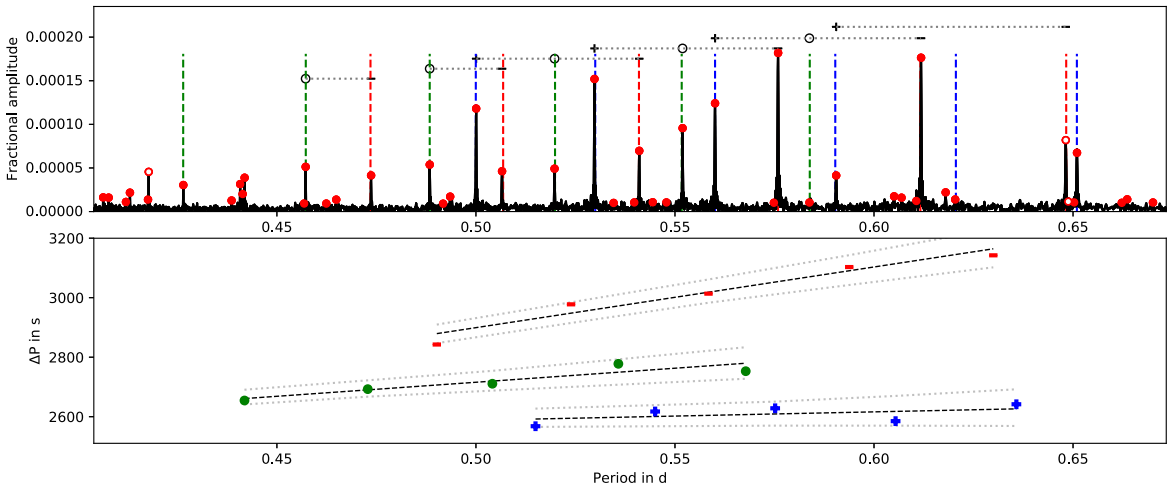

Figure A50. The period spacing patterns of KIC 10468883.

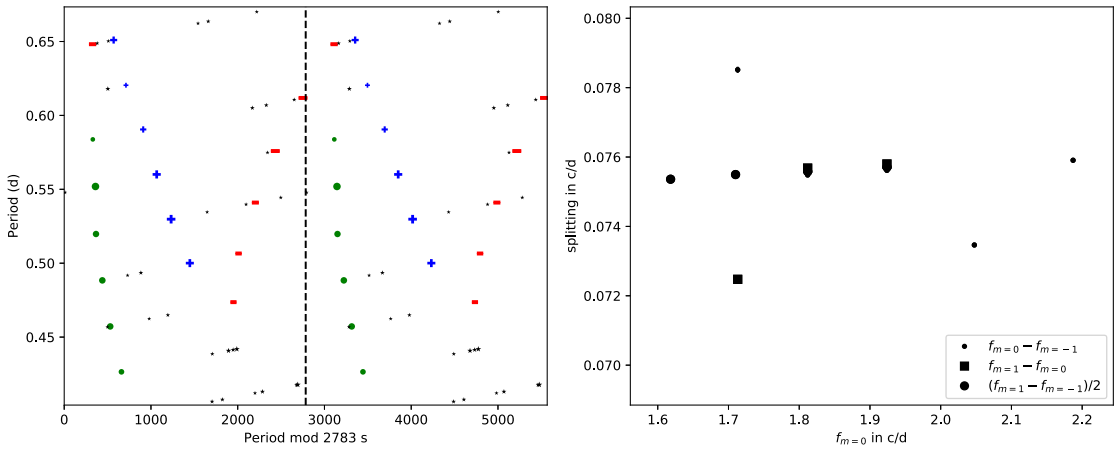

Figure A51. The échelle diagram and the splitting variations of KIC 10468883.

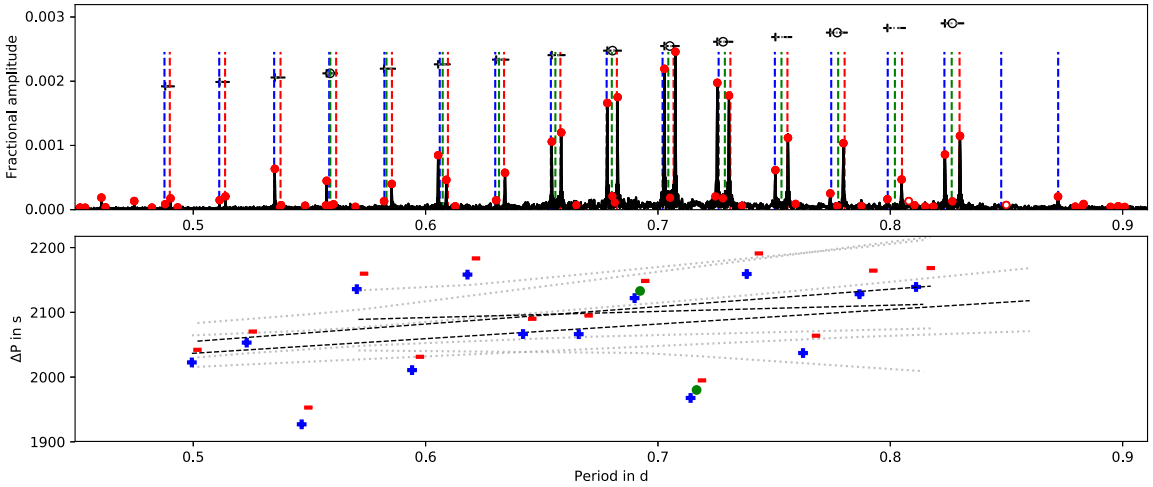

Figure A52. The period spacing patterns of KIC 11145123.

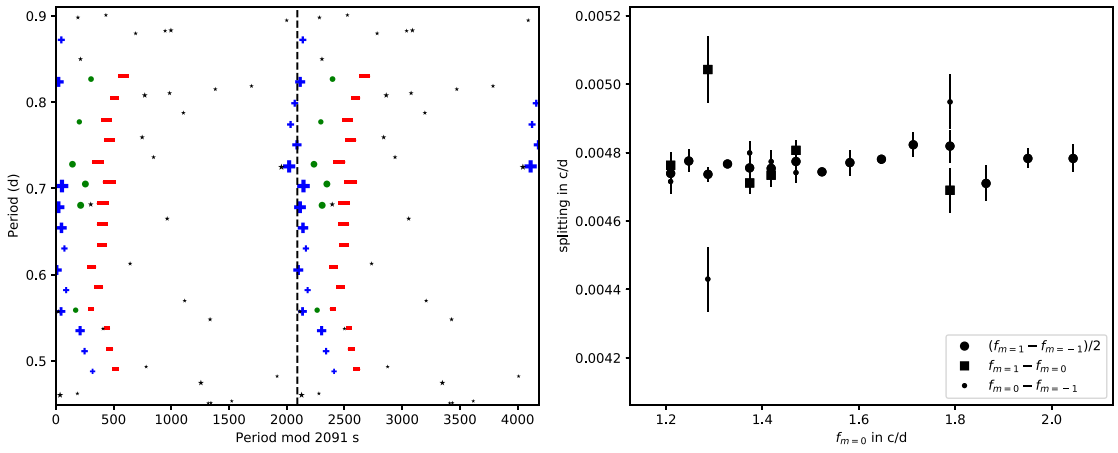

Figure A53. The échelle diagram and the splitting variations of KIC 11145123.

This paper has been typeset from a TEX/LATEX file prepared by the author.